Development of a-/nc-Ge:H

Growth and characterization of a low bandgap material

by

Bilal Bouazzata

to obtain the degree of Master of Science

at the Delft University of Technology,

to be defended publicly on Friday July 24, 2020 at 10:00 AM.

Student number:	4372409	
Project duration:	August 1, 2019 – July 24, 2020	
Thesis committee:	Prof. dr. A. H. Smets,	TU Delft, Supervisor
	Dr. P. Manganiello,	TU Delft, Assistant Professor
	Dr. L. M. Ramirez Elizondo,	TU Delft, Assistant Professor
	Ir. T. de Vrijer,	TU Delft, Daily Supervisor

TU Delft

Acknowledgements

With this thesis I'm concluding a 6 year long journey at the TU Delft. Overall I'm thinking back on the experience and looking forward to starting a new chapter my life. But before I can do that, I'd like to express my thanks and gratitude towards those that have helped me in achieving this. As I certainly wouldn't have been able to on my own.

I'd like to start off with saying a big thank you to Arno Smets. Your availability and openness to respond to my (what some might consider as dumb) questions have really comforted me in the thought that any question is a worthwhile question to be asked. Your passion and enthusiasm for academics and this project have managed to grow on me over the past year, so much so that I'm hanging around for a bit longer.

I would like to express the biggest thank you to my daily supervisor Thierry de Vrijer. Your ability to discern between the different personalities of your loyal servants (read: MSc students) and treat them accordingly really makes you one of the best supervisors one could ask for. Be it a quick question or a reminder on topics that we had already discussed numerous times, you never hesitated in helping on short notice with a calming attitude. Without your guidance I'd probably still be stuck on week 1 trying to figure out how to put on my clean room suit. So thank you immensely, again, for your guidance and friendship throughout the past year.

Thank you to the technicians and process engineers Martijn Thijssen and Remko Koornneef. You are invaluable to all of the research that is going on in the PVMD group and that has really become apparent during my research, from learning how to use CASCADE to fixing countless problems with the measurements setup.

My dear friend and CASCADE companion Ashwath Ravichandran, thank you. Working with you has been such a fun and fruitful experience. You were the first person I'd turn to with any questions I encountered with regards to the thesis (and football) and always helped me out wherever you could. Your work ethics and humble attitude have shown me that I still have a lot of growth left in me, and for that I thank you.

Bilal Bouazzata

Abstract

The maximal conversion efficiency on a single pn-junction solar cell is calculated to be 33.7% at a band gap energy of 1.34 eV. The main reasons for this maximum are the non-absorption of low energy photons and the thermalization of high energy photons. To counter this, multi-junction devices can be constructed to make optimal use of the spectral range of the sunlight reaching the earth's surface. While the introduction of thin film multi-junctions based on silicon has managed to overcome the problem of spectral mismatching, photons with an energy below 1.12 eV are still not able to be collected. Where usually a high current density is traded off against a high open circuit voltage in multi-junction devices, the addition of a low band gap germanium-based bottom cell ($E_g = 0.67$ eV) could improve open circuit voltage without negatively affecting the current density in the device. The photon flux in the range of 0.67-1.12 eV is high enough such that a current density of 15.9 mA/cm^2 can be produced when they can be effectively collected. This current density is so high that it will never limit the output current of a multi-junction device, making germanium a very attractive material for studying and integration in structures where the low energy photons are not yet utilised.

This thesis is focused around the growth and characterization of hydrogenated germanium films for future use as active absorbers in multi-junction deivces. The influence of a set of deposition parameters on the morphological, optical and electrical properties of the films is studied with the aim of finding a deposition regime where device quality germanium films can be produced within the CASCADE reactor in the EKL clean room. The thin films are all be deposited using the RF-PECVD technique. Uniformly deposited Ge:H films under a stable plasma can be deposited in CASCADE in the range of 1-5 mbar pressure and 5-30 W RF power at a fixed electrode distance of 20 mm. The films start to crystallize and form nc-Ge:H at a pressure of around 3-4 mbar and an RF power of 15-25 W when the germane precursor gas is diluted with hydrogen in a ratio of 1:400. A strong correlation between the refractive index and the presence of post deposition oxidation is investigated. Films with a low refractive index are characterized as having a low material denisty, making it easy for ambient water molecules to diffuse into the lattice and react with germanium dangling bonds present there. By studying the effect and extent of the post-deposition oxidation on other film properties it was found that the activation energy of the films decreases to values as low as 50 meV. Despite this, due to a significant decrease of the σ_0 by 1-5 orders of magnitude, the dark conductivity is found to decrease by 1-3 orders of magnitude. With a high photo/dark conductivity of 5-6 as a result. These results have led to the belief that the formation of Ge-O bonds in the films decreases the amount of defective states in the film, but that the defect states are moved up to an energy level closer to the conduction band. The presence of Ge-O bonds also inhibits the development of low band gap absorbers as seen by the low E_{04} optical band gap. In the denser films without oxygen contamination, the lowest E_{04} that has been reported is 1.2 eV along with a Tauc gap of 0.93 eV and a photo/dark conductivity ratio of 3.4.

Contents

List of Figures

List of Tables

1

Introduction

1.1. Introduction

One of the core issues in human development has always been the procurement of a reliable energy. In today's world, electricity and fuel have become such an integral part of life that it would be hard to imagine our lives without them. The main sources of energy are petroleum, earth gas, hydropower, nuclear power and coal. In 2017 the world's total primary energy consumption was estimated at $0.162 \cdot 10^{15}$ kWh; an increase of 50% when compared to the primary energy consumption in 1990 [1]. The declining extraction rates of fossil fuel sources along with the detrimental impact their use has on environmental factors has changed our perspective on a conventional energy source towards a more future-focused outlook where integration of PV (photovoltaics) and wind energy has become the norm.

A growth of interest in PV as a reliable energy source sprouted in the 70's after the oil crisis. It was realized that a significant amount of electrical energy could be obtained from sunlight which could massively lower the need for burning up fossil fuels or nuclear fission. One of the main reasons and selling points for PV is the availability of solar power all over the world. This means their use in applications could be endless. To name a few, PV has been used as a source of electricity for applications such as powering satellites, peak load assistance in the grid, remote area powering and wide range communication [2] [3]. It is the aim and belief of many around the world that the use of photovoltaic technology could contribute to greatly improving both energy security and the level of carbon dioxide emissions into the atmosphere.

Crystalline silicon (c-Si) is one of the most widely used semiconductor material in photovoltaic (PV) technology to manufacture solar cells. c-Si occupies more than 90% of the total PV market revenue [4]. c-Si solar cells can be made either from single (c-Si) or multi-crystalline (mc-Si) silicon material. The reason for c-Si solar cells holding such a large market share within the PV sector is primarily due to the fact that silicon is one of the most abundant materials in the world's crust as an ore in the form of quartizite. In addition, it is also one of the most studied materials in the world, making extraction and purification method of silicon readily available and cheap [5]. The energy gap of silicon is moderate (1.12 eV) resulting in an intrinsic carrier concentration of about 10^{13} cm^{-1} [6]. This is relatively low which leads to a small leakage current in PV devices. Lastly, silicon dioxide can also be used as an insulator and passivation layer in these types of devices.

Despite the lowered costs and generally high efficiencies of using c-Si single junction devices, the biggest drawback of using them is a relatively poor light absorption. As a result of the low absorption coefficient of c-Si, c-Si cells must be made relatively thick in order to absorb enough of the solar spectrum and have a reasonable efficiency [7]. The increased thickness of the c-Si layer requires high quality device-grad silicon with very long carrier lifetimes. As a result the ingots from which the wafers are cut are expensive to produce. To achieve lower costs for commercial purposes and wider scale integration of PV, a need for different semiconductor technologies for PV applications is needed. One of the solutions that has surfaced is thin film technology.

In terms of fabrication cost, thin film technology has a significant advantage over c-Si in a large scale. Due to their increased absorption coefficient over a similar spectral range, thin films solar cells can be made about 100 times thinner than c-Si solar cells. In addition, they are generally deposited onto low cost substrates at decreased temperature [8]. This makes fabrication both cheaper and easier from a commercial standpoint. Thin film technology also supports use of materials with a higher impurity concentration. Many materials are investigated for integration in thin film PV applications. The semiconductor systems that have attracted the most attention are CdTe, Si, CIGS and GaAs thin film technologies. Each with their own advantages and applications.

Cadmium telluride is the most widely used semiconductor for thin film solar cells. CdTe thin films have a peak recorded efficiency of more than 22.1%. CdTe cells are also shown to have the quickest payback time (the time it takes for the solar panel's electrictity generation to cover the cost of purchase and installation) of any of the thin film technologies [9]. Amorphous silicon (a-Si) thin films are the older and most studied type of thin film. Generally a-Si is cheaper to manufacture than c-Si and other semiconductors. Its earlier mentioned abundance and non-toxicity have made it a popular choice for use as thin film solar cells. The average efficiency of a-Si cells is however very low, not reaching more than 10% [10]. Copper indium gallium selenide (CIGS) is another type of semiconductor suitable for thin film solar cells. Efficiencies as high as 21.7% have been recorded [11], making CIGS a promising semiconductor material for solar cells and thin film technology. CIGS has however been traditionally more expensive compared to other cells that are commercially available, limiting their practical use. Lastly Gallium Arsenide (GaAs) solar cells have been produced with record peak efficiencies close to

30% on lab scale [12]. The high cost has been a major factor in the limitation of GaAs solar cells for practical uses, making them viable for a niche of use in spacecrafts and satellites.

A further approach in order to increase the efficiencies of thin film solar cells is the use of a multi-junction structure. In a multi-junction device the absorber layers are stacked according to their relative bandgap energies. By stacking the absorber layers, both thermalization and sub bandgap can be minimized in order to achieve ground breaking peak efficiencies [13]. Group IV multi-junction devices are most commonly based on a-Si, alloys of a-Si such as silicon-germanium (a-SiGe:H) and microcrystalline silicon (μc-Si:H) to form double junction (micormorph tandem) and triple junction devices.

1.2. Aim & Outline of the Thesis

The use of germanium (Ge) as a bottom cell absorber in multi-junction structures can be justified by looking at the energy difference between silicon and germanium. Germanium has a much lower bandgap energy of 0.67 eV than silicon (1.12 eV). Since the bottom cell of group IV semiconductor based multi-junction devices is usually made up of microcrystalline silicon, photons with energies in the infrared part of the spectrum (energy below 1.12 eV) are not collected. By introducing a low bandgap thin film PV junction based on germanium, the solar spectrum in the range of 0.67-1.12 eV can be utilised to increase the open circuit voltage by an additional 0.2-0.4 V. A great advantage of using such a low bandgap bottom cell is that it will never be the current limiting factor since a large number of photons are present in the infrared part of the spectrum. Due to the high current density available in the Ge bottom cell (because of the high photon flux at 0.67-1.12 eV), the bottom junction will also not limit the fill factor (FF) of the multi-junction device. This allows the germanium bottom cell to have a higher defect density compared to the other junctions.

The aim of this thesis is to deposit device quality Ge:H absorber layers that can be used for integration in multi-junction devices. The Ge:H films will be deposited using the plasma enhanced chemical vapor deposition (PECVD). The main focus of the thesis lies in using the different deposition paramaters of the PECVD process in order to characterize their effect on the optical and electrical properties of the films. This is an essential first step towards depositing device grade Ge:H absorber layers.

Chapter 2 of this report treats the theory and background information necessary to understand and follow the choices made throughout this thesis. Chapter 3 serves to highlight all the necessary steps taken in preparing the samples for characterization. In Chapter 4 the different characterization techniques and ways in which the parameters are extracted are discussed. Furthermore, in Chapter 5 a complete deposition window for the Ge:H samples is given. Chapter 6 presents the characterization results, investigating on the effect that various deposition parameters have on the optical and electrical films properties. Lastly, the thesis report is concluded in Chapter 7 where the most important results/trends of this work are summarised along with recommendations for future research in the context of Ge:H characterization.

2

Theoretical Background

This chapter highlights some basic concepts regarding photovoltaic technology and its fundamental building block, the semiconductor.

2.1. Solar Irradiance

The sun reaches a temperature of well over 5500 K and thus emits a spectrum of light that stretches from the deep ultraviolet to the far infrared parts of the electromagnetic spectrum. Releasing about $3.8x10^{26}$ W of power, on earth, the portion of light received from the sun equates to roughly $12x10^{16}$ J of energy per second [14]. On its own, this is enough to reach the annual energy quota of the entire world within a mere hour of time. The solar spectrum is shown in Figure 2.1.

Outside of the Earth's atmosphere, the solar irradiance reaches a value of 1360 W/m^2. Compared to a power density of 62 MW/m^2 at the surface of the sun, it's readily seen how distance attenuates the power radiated from the sun. As can be seen in Figure 2.1 the incident power is highest in the visible part of the spectrum, tapering off into the IR region. The spectrum that reaches the earth, denoted by AM0, is further attenuated due to various absorbing and scattering agents (predominantly O_2, O_3 and N_2) in the Earth's atmosphere. The optical path through the earth's atmosphere to its surface is dependent on the decline of the earth to the sun, described by the angle of the sun to the zenith. As a result, Air Mass (AM) is introduced as a measure of the earth's atmospheric attenuation and is given by Equation 2.1.

$$AirMass = \frac{Optical\,path\,to\,the\,sun}{Path\,length\,if\,the\,sun\,is\,directly\,overhead} \tag{2.1}$$

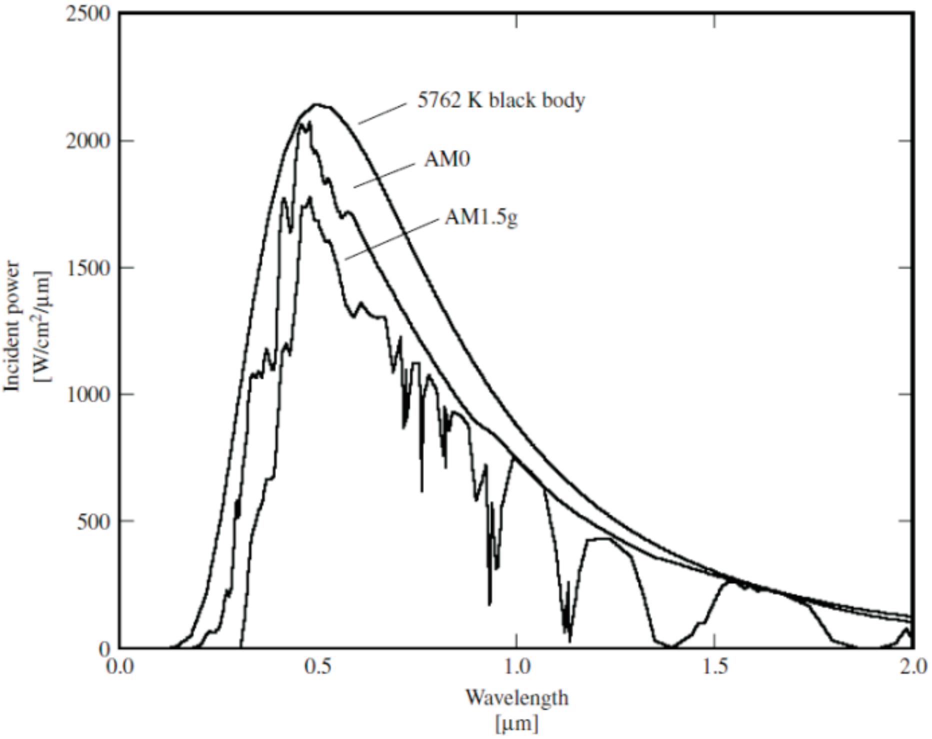

Figure 2.1: The radiation spectrum for a black body at 5762 K and its AM attenuations [15].

As mentioned earlier, the solar spectrum outside the earth's atmosphere is referred to as AM0. At noon, on a cloud-less day when the sun is directly overhead, the spectrum can be described AM1. When the earth's surface is positioned at angle of 48°, the spectrum is is referred to as AM1.5. The AM1.5 spectrum is normalized at an irradiance of $1000W/m^2$ and is a standardized spectrum used for the purposes of solar cell and film comparisons. It should always be noted that the true irradiance varies with weather conditions and most importantly the position of the sun to the earth.

2.2. Semiconductor Physics

The principle of photovoltaics relies heavily on the concept of light wave-particle duality in quantum mechanics. Essentially light can be described as a wave with all its characteristic qualities but more importantly as a flux of photons. These elementary particles carry an energy E_{ph} equal to:

$$E_{ph} = hc/\lambda \tag{2.2}$$

Where h is the Planck constant, c is the speed of light and λ is the wavelength of the incident light.

2.2.1. Atomic structure

In order to more properly understand the growth and characterization of Ge:H thin films it is necessary to differentiate between crystalline and amorphous group IV semiconductors. In a perfect crystal, each atom shares a covalent bond with four neighbouring atoms at an equal spacing and bonding angle. This type of bonding structure is called a diamond cubic coordination as shown in Figure 2.2a. If there is no long range structural order, the material is referred to as amorphous. An amorphous network is shown to be a continuous random network. While the long range order between the two lattices is completely different, they still share very similar short range order. This leads to the two materials still being similar in energy state band configurations [10]. This will be further discussed in Section 2.2.2.

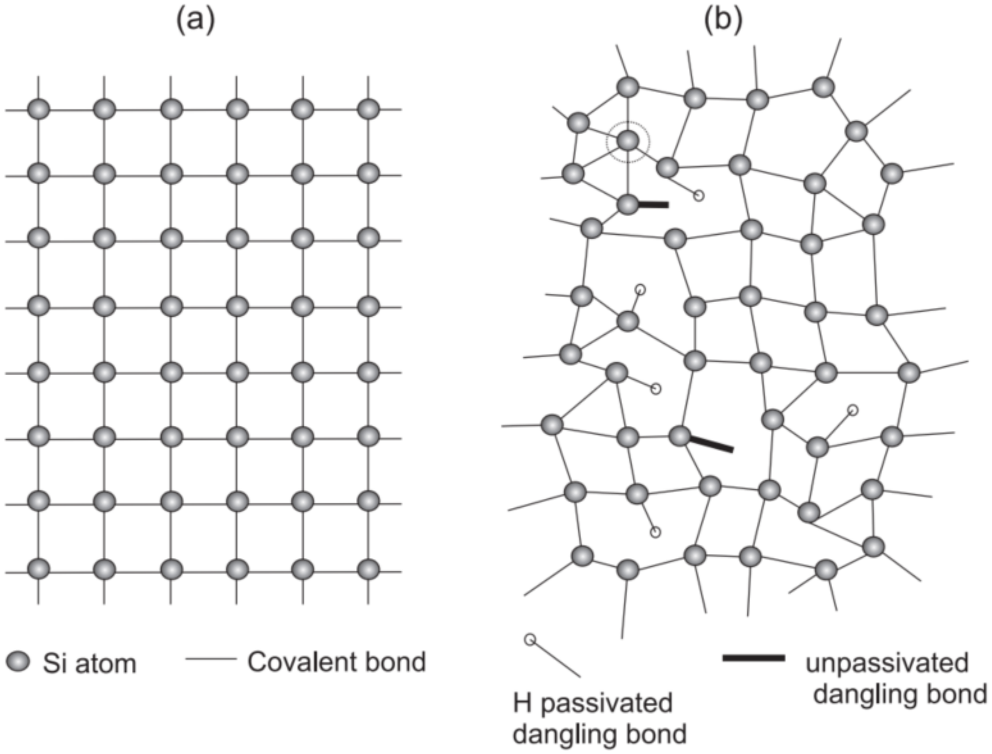

Figure 2.2: Diamond cubic lattice in group IV semiconductor Si in (a) c-Si form and (b) a-Si:H form [16].

A five-fold point in the lattice with an extra bond is called a floating bond while a three-fold point in the lattice with an upaired bond is called a dangling bond. Both of these bonds (possibly introduced by doping, irregular bonding angles/lengths or contaminants) are considered as defects in the crystal lattice and will result in a deviation from the ideal structure. In addition, they serve as possible sites for recombination which proves detrimental to solar cell performance. Typically, amorphous germanium has a defect density of about $10^{22}\ cm^{-3}$ [17] which can be further reduced by passivating the dangling bonds with hydrogen atoms. The resulting material is called hydrogenated amorphous germanium (a-Ge:H). After passivation the defect density can be brought down to $10^{18}\ cm^{-3}$ [18]. It should be noted that this density is still 2-3 orders of magnitude larger than in a-Si:H leading to the poorer opto-electrical responses of a-Ge:H compared to a-Si:H.

2.2.2. Band Theory

When many atoms are brought together into a lattice, their energy levels split forming essentially continuous bands of energies [19]. As a result, the electrons will move to occupy these particular sets of well-defined energy levels. These energy levels are defined through the periodicity of the crystal lattice and the molecular bonds between atoms. Every material has its own particular energy band structure and this is again defining for a material's electrical and optical characteristics when measured. The most filled energy band called the valence band (VB) and the most empty energy band called the conduction band (CB) can be used to distinguish between metals, semiconductors and insulators.

The band energies of metals usually overlap such that electrons are able to move freely in the lattice. This makes for the good conductive qualities of metals. In insulators, the VB and CB are sufficiently spaced from one another by a forbidden region. This region is defined as the bandgap energy (E_g). As such the resistivity of these materials is very high at low temperatures. Semiconductors are similar to insulators in the sense that they are defined by a bandgap energy. What differentiates them is the energy level of E_g. In semiconductors the bandgap is small enough in the range of 0 eV to 3 eV [19], such that an external amount of thermal/optical energy is able to excite electrons form the VB into the CB. When this happens an increase in the semiconductor's conductivity can be measured as a result. These band structures are depicted in Figure 2.3.

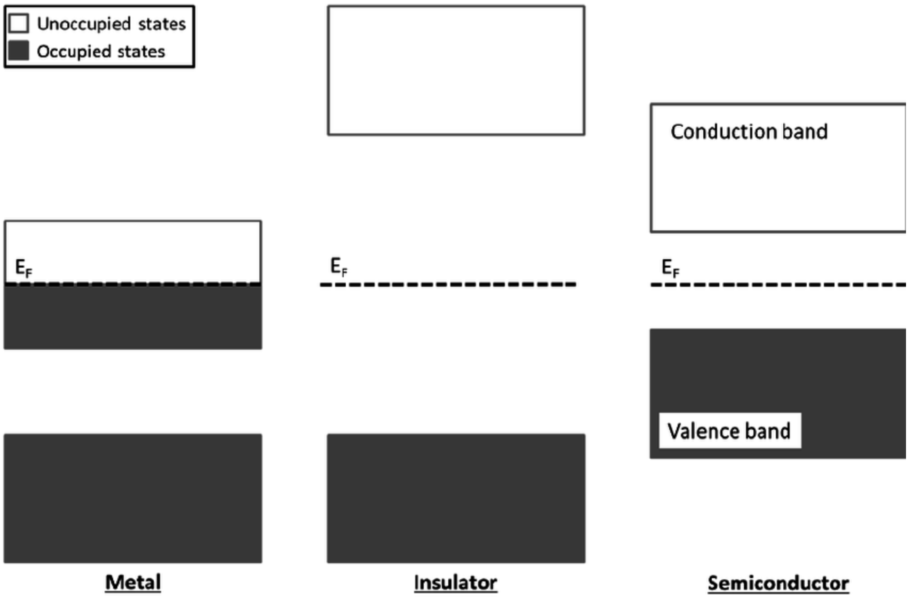

Figure 2.3: Band structure of metal, insulating and semiconducting solids [16].

The appeal of using semiconductors as material for PV technology becomes apparent when considering their characteristic E_g. Using the periodicity of the crystal lattice, it is possible to calculate the different possible energy states [20]. This is also the reason why band diagrams are plotted as a function of k, a space dependent wave function important in crystal vibrations [20]. Materials where the maximum and minimum of the VB and CB occur at the same value of k are called direct semiconductors. In direct semiconductors a photon with at least an energy of E_g is able to excite an electron into the CB. In materials where the peaks of the CB and VB are not aligned with the wave vector k, a change in momentum is needed in addition to a photon to promote the electron into the CB. See Figure 2.4.

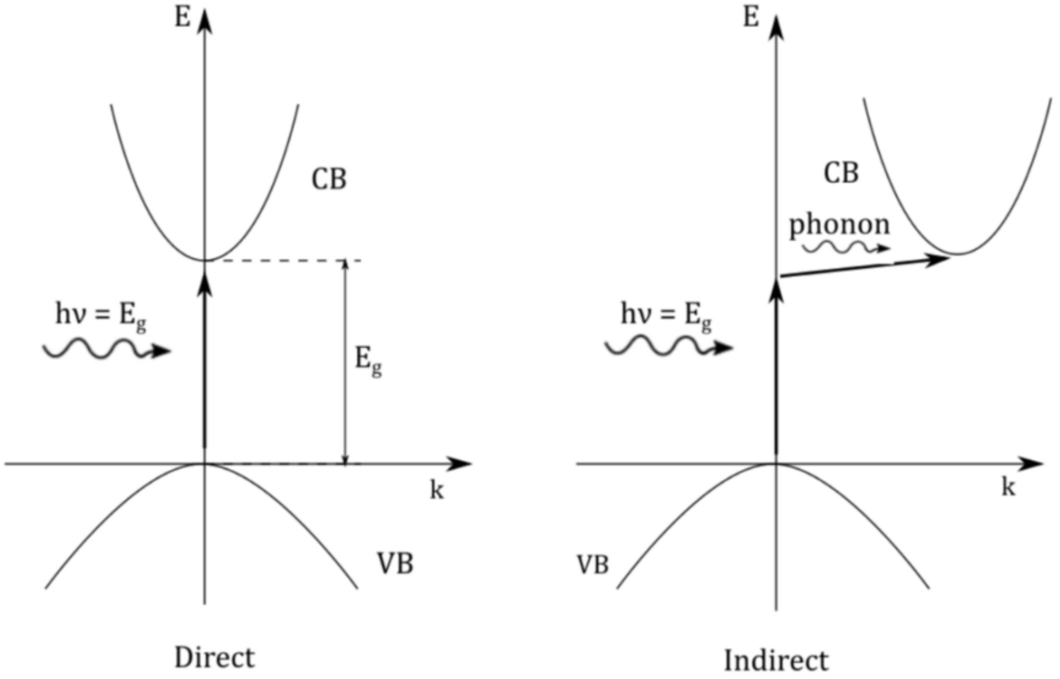

Figure 2.4: Direct and indirect VB-CB transitions [21].

This variation in momentum can be provided by a phonon, a collective vibration in the lattice of the semiconductor [22]. For solar cell technology the main point of interest in the difference between indirect and direct semiconductor materials is in their absorption of sunlight. In indirect semiconductors, because of the need for an additional phonon, the probability of electron excitation becomes much smaller. This leads to a lower portion of the spectrum being absorbed by the films when compared to direct semiconductor materials (at equal thickness and E_g). This would usually be overcome by increasing the thickness of the absorber layer which could be seen as a downside in some solar cell technologies. A larger thickness of the absorber layers means that the minority charge carriers are required to have a higher diffusion length [23].

Looking back at Equation 2.2 it becomes possible to connect the solar spectrum in Figure 2.1 the E_g of a semiconductor. Since each wavelength corresponds to a certain photon energy and the semiconductor will only absorb photons with $E_{ph} \geq E_g$, the bandgap energy now represents a lower bound for absorption of these photons. Silicon, one of the most widely used semiconductors for solar cell technology, is depicted to have a bandgap at 1100 nm making it apparent that a large part of the spectrum can still be used for excitation of electrons into the CB. And thus light absorption could be improved in multi junction solar cells through the implementation of a Ge based bottom cell [24].

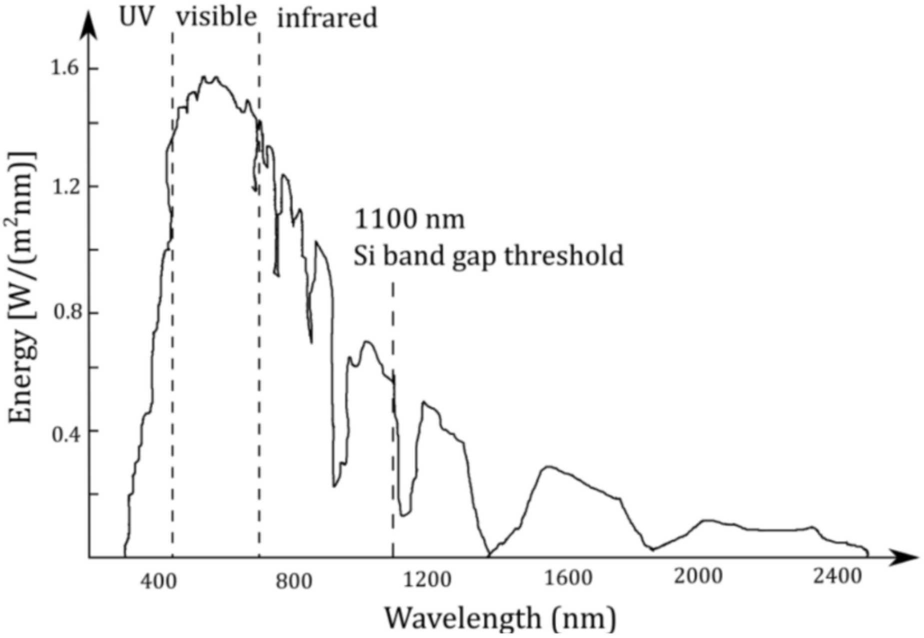

Figure 2.5: Solar spectrum showing the lower bound at which Si absorbs energy because of its 1.12 eV bandgap. Whereas Ge has a much lower bandgap at 0.67 eV [15].

2.2.3. Density of States

The density of states (DOS) and its distribution are of great importance in understanding the opto-electrical properties of a semiconductor. The conceptual idea behind it is that when an electron is joined to a perfect lattice, it can be seen as occupying a well-defined finite energy level. Over a range of energies, the amount of available sites per unit volume for electrons to occupy at each energy level is referred to as the density of states. For an ideally structured, intrinsic semiconductor the density of states of the semiconductor is very well defined. Additionally, no available energy states are present within the bandgap. In amorphous networks such as a-Ge:H, it becomes extremely difficult to accurately calculate the DOS.

Due to the random long range order of amorphous networks, exponential distributions of energy states from both the CB and VB spread into the bandgap [25]. These are called band tails and introduce possible energy states in the bandgap of the semiconductor where these would normally be forbidden. These tail states are described by:

$$N_{TC} = N_{C0} exp \frac{E_V - E}{E_{urc}} \tag{2.3}$$

$$N_{TV} = N_{V0} exp \frac{E - E_V}{E_{urv}} \tag{2.4}$$

Where E_{urv} and E_{urc} are the characteristic widths of the valence and conduction band tails respectively. These tail widths are also commonly described by the Urbach energy, a measure for the inverse slope of the band tails. The Urbach energy becomes a very important measure for determining the quality and disorder in the material. A low Urbach energy (steep slope) readily implies less disorder and low tail width E_{urv}, E_{urc}.

As mentioned earlier, point defects introducing floating or dangling bonds can also create new energy states in the region between the CB and VB. These energy states are referred to as localized states. Because of their placement in the bandgap, it now becomes very difficult to accurately determine a single accurate bandgap energy for the amorphous material. Figure 2.6 shows the standard model for the DOS in amorphous semiconductors.

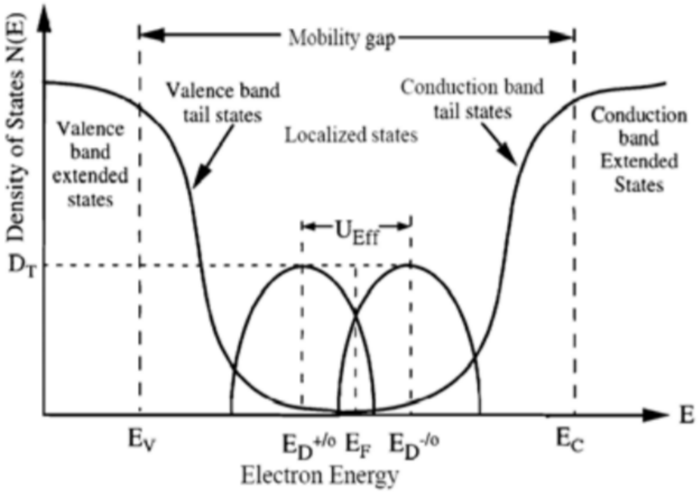

Figure 2.6: The standard model for DOS in amorphous semiconductors [26].

The model in Figure 2.6 shows the valence and conduction band tail states introduced by the random network of the lattice including the localized states around the Fermi level introduced by dangling bonds in the lattice. The charge state of these localized states depends on the location of the Fermi level in the energy gap. The dangling bond states are referred to as negative (D^-) or positive (D^+) depending on if the Fermi level is closer to the CB or VB respectively. If the Fermi level is in the middle of the energy gap, these defect states are referred to as neutral (D°)

Both localized states and the tail states play a crucial role in the determination of the quality of the thin films as they could trap electrons and promote recombination. By tuning and optimising the growth conditions of the a-Ge:H films, suitable low-defect material can be produced.

2.2.4. Staebler-Wronski Effect

A significant challenge in the design and application of amorphous thin film solar cells is overcoming the light induced degradation (LID) in the opto-electric properties, commonly known as the Staebler-Wronski Effect (SWE) [27]. It has been widely reported that the dark- and photo conductivity of a-Si:H decreases after the material has been exposed to sun light for a prolonged period of time. This happens as a result of an elevated defect density in the film. The changes in the electrical properties of the films were however found to metastable. This means that the degradation is (partially) reversible and can be countered by annealing the material at 150 °*C* [28].

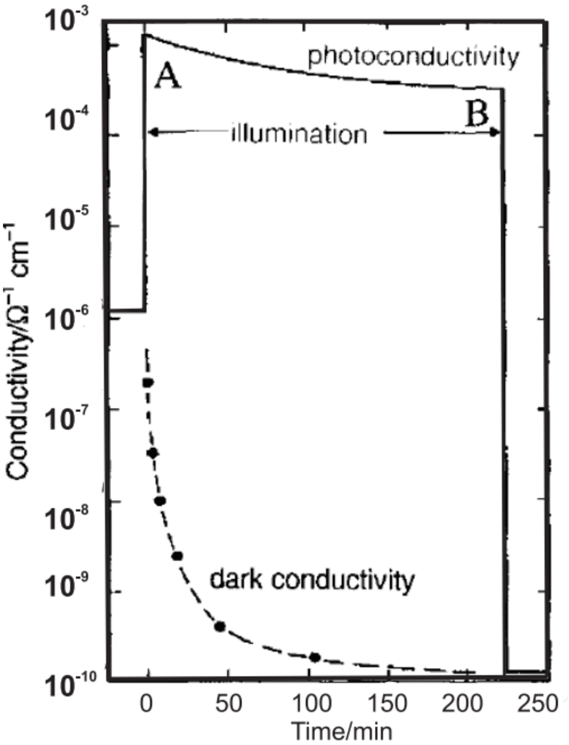

Figure 2.7: Photo conductivity and dark conductivity degradation as a result of light illumnation in a-Si:H [29].

While the exact nature of the SWE is still under discussion, it has been widely accepted that the defects are generated as a result of the breaking of weak/strained Si-Si bonds or through the emission of mobile hydrogen from the Si-H bonds. These metastable defects then act as recombination centers for free carriers, increasing the DOS in the regions between the VB and CB.

3

Sample Preparation

In this chapter , all the steps taken to deposit the thin films and prepare them for measuring are presented. Substrate cleaning, thin film deposition and metal contact annealing all form integral parts in preparing the sample for characterization.

3.1. Overview

All films are deposited on circular 10 cm, 500 μm thick (100) monocrystalline silicon wafer which were cut into quarter pieces for Fourier Transform Infrared (FTIR) spectroscopy measurements. Simulataneously, they are grown on 2 cm x 1 cm quartz substrates for Photothermal Deflection Spectroscopy (PDS) measurements and standard 10 cm x 2.5 cm Corning XG glass substrates for all remaining measurements. The thickness of the films and electrode distance in the reactor were kept constant at 80-120 nm and 20 cm respectively. All the other varying parameters will be mentioned in Section 3.3 and their influence of the growth of Ge:H films will be extensively treated in Chapter 6.

All of the samples were cleaned and grown in a class 10,000 clean room (ISO class 4) in the Elsekooij Laboratory (EKL) at the Technical University Delft. Figure 3.1 shows a flow chart of the several steps involved in preparing the samples for measuring.

3.2. Substrate Cleaning

Prior to growth, the glass substrates were solvent cleaned in the ultrasonic bath. The ultrasonic bath uses sonic waves to create bubbles in the solvent, thereby removing dust, finger prints and other contaminants from the surface of the substrates. This way the substrates are free of

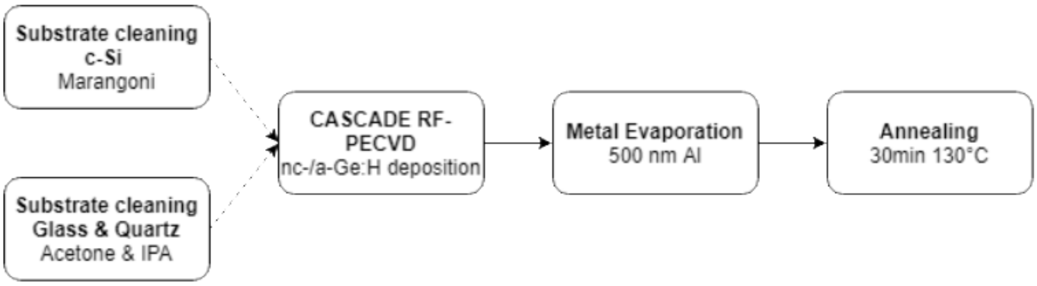

Figure 3.1: Flow chart of the sample preparation process for this thesis.

any residual dust or other contaminating particles that might influence the growth of the thin films [30]. The ultrasonic bath cleaning followed a standard procedure of a 10 minutes bath in acetone. Nitrogen gas was used to blow-dry the substrates after which they were cleaned for 10 minutes in an isopropanol (IPA) bath. The substrates were again blow-dried with nitrogen before being placed in the load-lock chamber (LLC).

In order to remove the native oxide layer on the c-Si wafers, they were dipped for 4 minutes in a 0.5% HF solution. The wafers were subsequently rinsed and dried using the Marangoni effect [31]. IPA is introduced into the bath on top of DI water in which the wafers are dipped. The IPA (low surface tension) diffuses into the DI water (high surface tension), creating a gradient of surface tension throughout the depth of the bath (surface having a low surface tension due to IPA and bulk having high surface tension due to DI water). As the wafers are pulled slowly upward through the interface, H2O is pulled away from the surface and the wafers are dried and cleaned.

3.3. Plasma Enhanced Chemical Vapor Deposition

Chemical vapor deposition (CVD) is a process that relies on chemical reactions between gaseous or liquid precursors with other reactants [32] in order to grow a film on a substrate. CVD has a lot of different types classified based on how the chemical reactions are initited but they all follow the same general set of steps as shown in Figure 3.2. The CVD process starts off with precursor and carrier gasses being introduced from the inlets into the reactor. These reactants approach the surface of the substrate and are chemically adsorbed. After that, the reactants diffuse across the surface of the substrate to a site which is energetically favorable for the growth of the film. Lastly any volatile by-products of the chemical growth process are desorbed into the main gas flow region and eventually pumped out of the reactor.

Plasma enhanced chemical vapor deposition (PECVD) is particular type of the CVD technique and thus also follows the main steps laid out above. A key difference to the general CVD

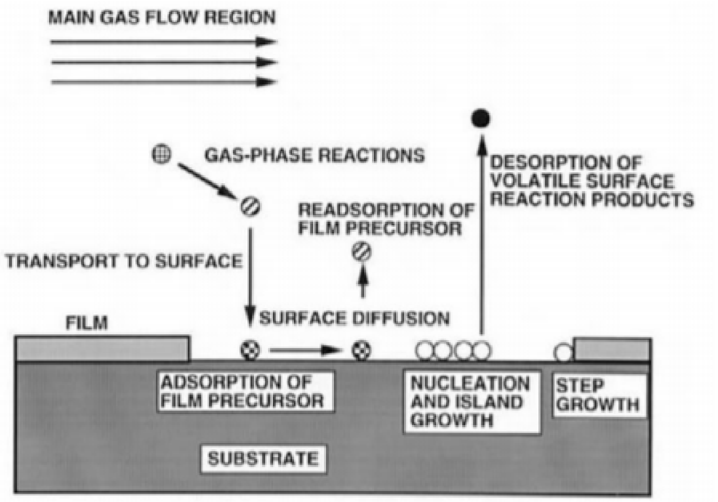

Figure 3.2: Schematic representation of transportation and reaction flows in CVD [33].

process is that a glow-discharge plasma (a plasma originating from a gas under low pressure) is used to stimulate the chemical reactions laid out above. In the majority of the PECVD processes, the plasma is excited by an external electric field which simultaneously serves as a path in which the electrons are able to accelerate. The energetic electrons are then able to induce different electron-impact processes as shown in Figure 3.3. Dissociation and ionization are the two most important processes in the plasma as they lead to the formation of chemically highly reactive radicals in the plasma that are able to attach to the substrate and grow the film. This process in relation to the growth of germanium films is explained in more detail in Section 3.3.1.

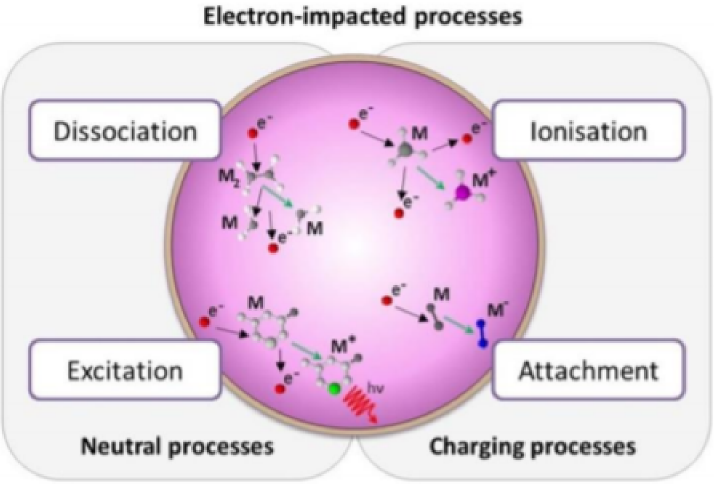

Figure 3.3: Electron impact processes in PECVD plasma [33].

One of the main advantages in using PECVD over other CVD techniques is the fact that PECVD is able to operate at much lower temperatures. This is due to electrons having a much higher energy compared to the other molecules in the plasma and as such their temperature is also much higher [34]. The temperature setting of the heater can be lowered as a result of this.

Figure 3.4 shows a schematic representation of a typical RF-PECVD system as used in this thesis. The PECVD system's main components are the gas inlet, heating chuck, power generator and housing. As such a number of parameters can be tuned for optimization of film growth.

- **Gas Inlet System:** Within the gas system, the available precursor gasses can be selected along with their flow rates F (sccm). The gasses used for the samples throughout this thesis are germane (GeH_4) and hydrogen (H_2). The ratio in between the precursor gasses' flow rates $D = F(H_2)/F(GeH_4)$ has a significant impact on the defect density and morphology of the samples. It has already been discussed how hydrogen inclusion can significantly reduce the localized defect densities for site of Schockley-Read-Hall (SRH) recombination. In addition it has been shown that the introduction of hydrogen during film growth can promote crystalline growth. Presumably through a complex process in which the bond angles and bond lengths are restructured by higher H_2 flow rates together with high chemical etching of weak amorphous bonds near the growing surface[35] [36].

- **Pressure:** The pressure which the gasses are under in the reactor can also be varied. Generally a higher pressure will lead to radicals in the gas with a lower average energy gain and thus the bombardment of the surface with these ions will lead to less structural damage [37] [38]. The higher pressure is also reported to induce a higher growth rate of the films [37]. It should be noted that the gas-discharge plasma relies on a low pressure regime and in the event that high pressure and power are coupled, polymerization of the gas molecules could happen outside of the substrate surface as will be discussed in Section 5.

- **Temperature:** It has already been discussed how a lower temperature is more favourable in industrial processes. It has been reported that the average growth rate increases with an increasing substrate temperatures while simultaneously increasing the grain size of the films [38] [39].

- **Power:** Increasing the RF power generally increases the dissociation rates in the plasma together with increasing the average energy of the ions.

The Ge:H samples that are presented and studied in this thesis have all been deposited in the RF chamber of the the Cascaded Arc Solar Cell Apparatus Delft Eindhoven (CASCADE) in the EKL class 10,000 room. The CASCADE PECVD setup can be seen in Figure 3.5.

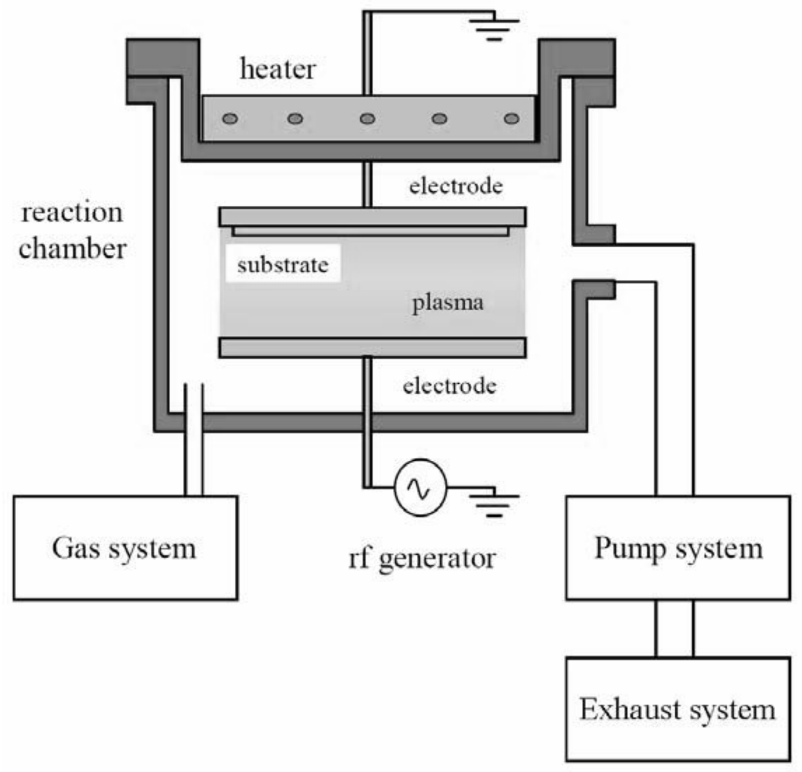

Figure 3.4: Schematic representation of an RF-PECVD system [40].

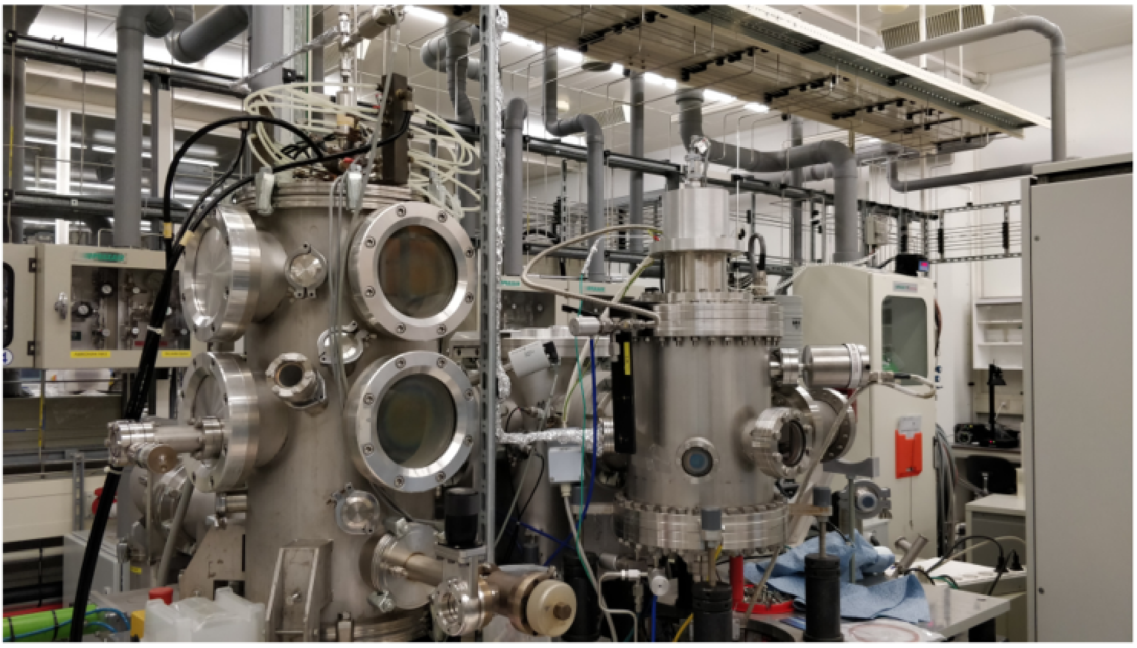

Figure 3.5: The CASCADE RF-PECVD system in EKL.

3.3.1. Ge:H Growth Chemistry

The growth mechanics of the thin films processed with PECVD, while difficult to observe and understand, prove to play a major role in the deposition of high quality material. Especially so in high growth rate depositions [41]. Later in this section a comparison will be drawn between Si and Ge, making it evident why Ge:H films have higher growth rates and how that affects their electrical characteristics. Achieving high growth rates with standard PECVD techniques has resulted in the deposition of films that are more prone to LID, especially in semiconductors alloyed with germanium [42]. The main cause being the inclusion of a lot of voids in the film. In PECVD using GeH_4 as a precursor, the main radical-creating reactions near the substrate that have been identified and studied are [43]:

$$e + GeH_4 \Longleftrightarrow GeH_3 + H^+$$

$$e + GeH_3 \Longleftrightarrow GeH_2 + H^+$$

$$H^+ + GeH_4 \Longleftrightarrow GeH_3 + H_2$$

Out of these, it is believed that GeH_3 is the most important and frequent radical (90%). Should the content of the other radicals in the plasma be high, the surface will be roughened and many voids will start to appear in the micro structure of the material [43].

As shown in Figure 3.2, the growth of a-Ge:H is propelled mainly by lateral diffusion of GeH_3 radicals along the surface until a suitable sight is found for cross-linking. When the radical finds an open site, the Ge-H bond at the site releases the H atom to attach to the radical. This was however found to be counter intuitive as the Ge-H bond breaking strength is equal to 2.99 eV while the Ge-Ge bond strength is lower at 1.9 eV. As such there is no reason for a radical near to the surface to break open its H bond and engage in cross-linking with a Ge atom. This model of group IV semiconductor growth proposed by the authors in [44] was then improved in [42] where not diffusion of radicals along the surface necessarily dictated the growth but rather the removal of the hydrogen bonded to the surface Ge atoms through extraction of the H atoms. After which the radicals can readily bond to the open sites. Following this logic, a high H_2 flow will lead to a large concentration of H^+ ions that are disturbing the Ge-H surface bonds and thereby also breaking them.The hydrogen ions are even shown to affect the bulk and removing H bonds from the surface, freeing up space for re-ordering of the now dangling Ge bonds. Leading to the behavior explained in the previous section where a high H_2 could increase the grain sizes/crystallinity in the Ge:H films. Should the surface hydrogen not be removed during the growth of the germanium films, new material will continue to grow around it instead of bonding to it, leading to a significant void count in the bulk of the sample.ies.

Comparing the bond breaking strength of Si-H (3.35 eV) to Ge-H (2.99 eV) and applying the theories laid out in the paragraph above, it becomes apparent that Ge:H growth will happen more rapidly than well-studied Si:H films. This should be kept in mind when exploring the processing window for good quality Ge:H films as a high growth rate could impede the tunability of the film properties. Most experiments performed in the growth of a-SiGe:H have shown that limitation on the growth speed is essential (especially since Ge alloying highly increases the rate of growth) in making good quality material. The basic techniques that have been used so far in limiting the growth rate are hydrogen dilution, substrate biasing (E-field can lower ion bombardment) and basic PECVD control such as pressure and temperature variation [45].

3.4. Metal Evaporation and Contact Annealing

In order to perform electrical measurements on the films, metal contacts are deposited on the Ge:H samples. To this end, the metal evaporation technique was used. A high intensity electron beam is aimed at a piece of metal that is present in a crucible. The metal inside the crucible heats up and evaporates when the melting point is reached. Masks are used to make sure the contacts are deposited with the correct dimensions onto the samples. A schematic of the metal evaporation process is shown in Figure 3.6. For this thesis, all Al contacts have been deposited in the PROVAC 500 at a thickness of 500 nm. As a last step in the sample preparation process, all films with contacts are annealed in an oven at 130 °C to ensure a good ohmic connection between the contacts and film.

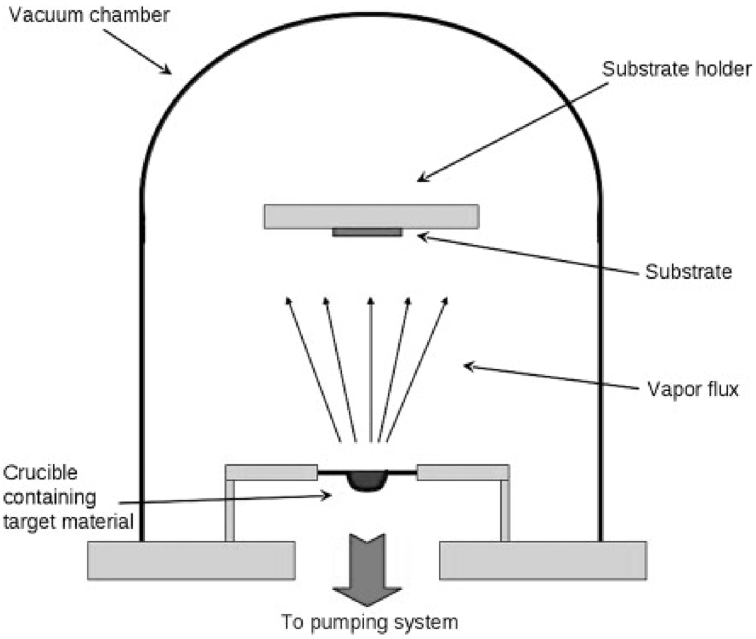

Figure 3.6: Metal evaporation for the deposition of contacts [46].

4

Thin Film Characterization Techniques

The main characterization methods used in the thesis and their uses are described in this thesis. For each method, the fundamental physics behind the characterization technique is explained following a detailed breakdown of paramater extraction and their interpretation. For clarity, the characterization methods have been split up into two categories, optical (no metal contacts need) and electrical (metal contacts needed).

4.1. Optical Characterization

4.1.1. Spectroscopic Ellipsometry

Spectroscopic Ellipsometry (SE) was chosen as the main method to measure the optical properties of the processed films. A J.A. Woollam variable angle M-2000D Ellipsometry system was used to do the measurements. SE is a fast, non-destructive method for characterizing thin films and multi-layered semiconductors. The basic working principle of SE is that the change in polarization state of light that has been reflected from a sample is measured. One of the many advantages of using SE is that the film does not have to be highly reflective to do the measurement. Figure 4.1 shows two ways in which light can be polarized.

Light can be parallel polarized (p-plane) or perpendicular polarized (s-plane). The ellipsometry setup measures the change in polarization of the light through the ratio of the p- and s- components in the reflected light (denoted ψ) and the difference in phase between the two different components (denoted Δ). Thee parameters are interrelated through:

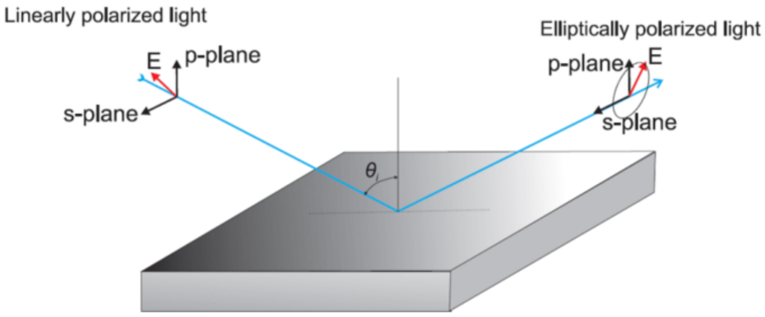

Figure 4.1: Interaction of polarized light with a sample being measured [21].

$$tan(\psi) \cdot e^{(i\Delta)} = \frac{r_p}{r_s} \tag{4.1}$$

With r_p and r_s the reflectivity of the respective polarized light components. An optical model is then built in the software in order to generate the optical data of the material. Different optical functions/oscillators can be added to the model such as the Tauc-Lorentz oscillator in order to accurately model the absorption in the Ge:H films. The accuracy of the fit produced by the software is expressed through the mean square error (MSE) which signifies the overall error in the data to the fitted model. A lower MSE means a better agreement with the fit and more accurate results.

Thickness and Refractive Index

As mentioned earlier, the thickness of the films was kept constant at 80-120 nm. SE gives a very accurate reading of the actual thickness of the films. With the thickness d of the film known, the growth rate can be calculated and can be plotted against various other deposition parameters to see their influence on the growth process of Ge:H.

The complex refractive index of a material is denoted as (n+iκ) with n the real part and κ the imaginary part. By reporting the real part of the refractive index n in the absorption range ($E \leq E_g$), a great insight into the comparative densities of the films can be gained [47]. With a higher refractive index implying a generally more dense material has been process. The refractive index is also hugely important in its relation to the absorption coefficient of the film:

$$\alpha(\lambda) = \frac{4\pi\kappa(\lambda)}{\lambda} \tag{4.2}$$

With λ the wavelength of the measured light. The absorption coefficient can be used to readily see how absorbing films compare at different wavelengths. An important parameter that reflects this is the E_{04} optical bandgap. It is the wavelength (or corresponding energy) at which the absorption coefficient of the film equals 10000 cm^{-1}. From Figure 4.2, the importance and practicality of this parameter can be seen. On a log plot, for most of the Ge:H samples, the absorption coefficient starts to drop sharply in value. This shows that the E_{04} is a reasonable approximation to the mobility gap of the material as in an ideal structure the absorption coefficient would drop sharply to zero around this E_{04} 'knee'. For materials where the slope in the absorption coefficient is flatter, the E_{03} can be specified in a similar manner to the E_{04} gap.

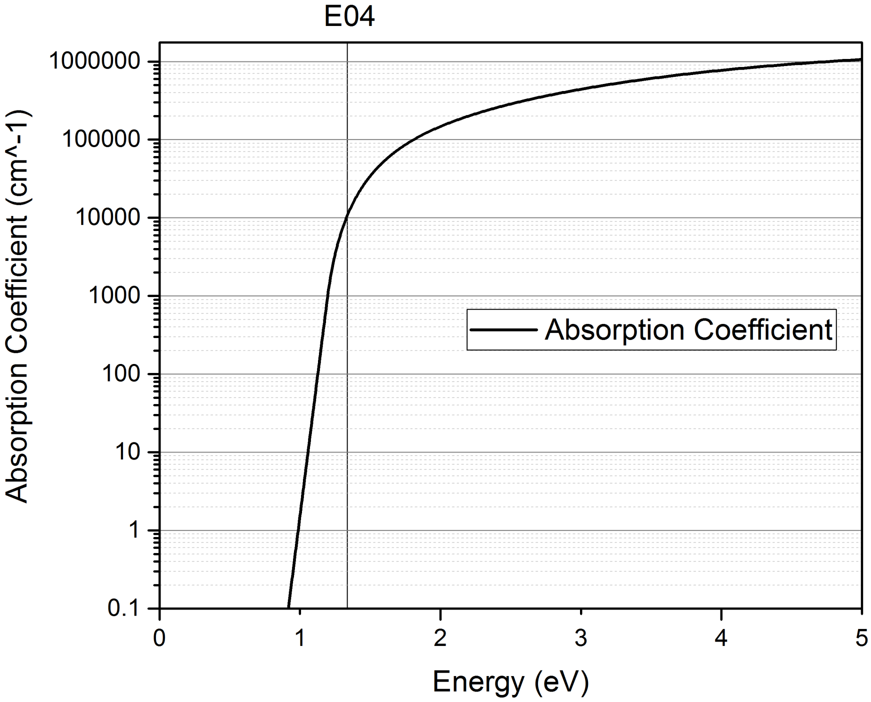

Figure 4.2: Derivation of the E_{04} optical bandgap from the absorption coefficient.

Tauc Gap

As mentioned earlier in Section 2.2.3, due to the random nature of the lattice structure in amorphous samples, a clear bandgap energy cannot be determined. To approximate the bandgap in amorphous structures, many different methods have been proposed. For this thesis, an approximation of the mobility gap is given through the Tauc gap E_{tauc} derived from the absorption data.

E_{tauc} is derived by restructuring the absorption data as:

$$E_{tauc} = (\alpha h \nu)^{\frac{1}{2}} \tag{4.3}$$

And plotting it as a function of the energy. With α the absorption coefficient, h Planck's constant and ν the frequency of light. By fitting a line through the straight part of curve, E_{tauc} can be extracted as the point of intersection of the fitted curve with the x-axis.

4.1.2. Photothermal Deflection Spectroscopy

Photothermal Deflection Spectroscopy (PDS) is an optical characterization tool based on detecting the deflection of a laser beam aimed directly past the sample surface when the sample is heated periodically. The Ge:H samples deposited on quartz substrates are dipped in a non-absorbing liquid Perfluorohexane Fluorinert (FC-72). When the incident laser is absorbed in the sample, the built up heat is transferred to the FC-72 liquid and the resulting thermal waves induce a change in the refractive index of the area near the sample, thereby deflecting the probing laser beam. The amplitude of the oscillating laser beam is detected with the help of a position detector and measured through a lock-in amplifier. The lock-in amplifier is referenced to the frequency of the incident light beam and hence its measurement is proportional to the amount of light that is absorbed in the sample. Highly absorbing Carbon nanotubes (CNT) layers aremeasured prior to the thin film simple for use as a reference layer in normalizing the PDS spectra [48]. PDS allows for the determination of the optical absorption of the films at energy levels close to and below the bandgap where SE measurements and generally less sensitive. PDS measurements thus serve as a complementary measurement to SE where the same parameters such as E_{tauc} and E_{04} can be extracted. The PDS setup used for this is shown in Figure 4.3. Here K1-K5 denote the positioning screws for the sample (placed in S) and DR/DT/DB/DA are the detectors that measure the R-, T-, B- and A-spectra respectively.

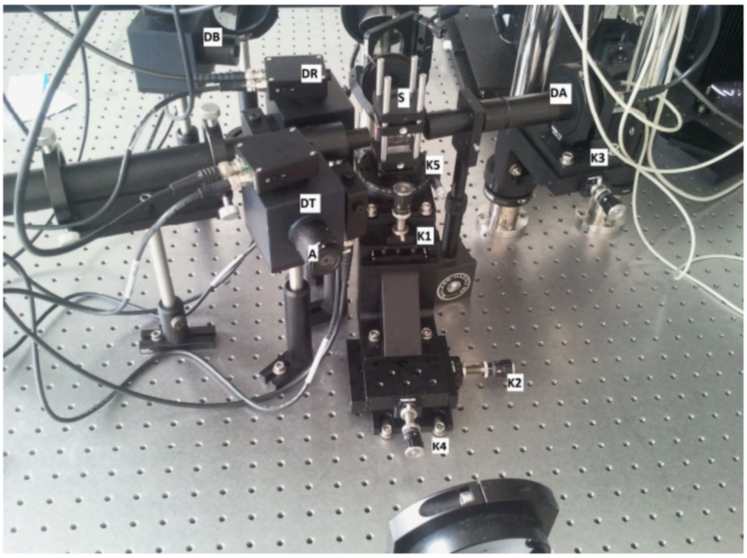

Figure 4.3: PDS measurement setup in the TU Delft PVMD group.

4.1.3. Fourier Transform Infrared Spectroscopy

Fourier Transform Infrared spectroscopy (FTIR) measures the absorption at different wavelengths of light in the infrared region on of the spectrum (400-4000 cm^{-1}). When the frequency of the infrared light is equal to the resonance frequency of a bond or group vibrating in the material, the light is absorbed. As such by looking at the transmittance/absorption of the IR light, the atomic bonds in the film can be detected and quantified. The biggest consideration in FTIR spectroscopy is that the only bonds that are detectable (FTIR active) are those that create a dipole moment when vibrating.

The FTIR spectra of the Ge:H films were corrected for the absorption of the c-Si wafers by measuring the substrate with no deposition. The absorption spectra from the FTIR were baseline corrected and subsequently the absorption peaks in Table 4.1 were fitted with multiple gaussian functions in Fityk freeware. An example of the fitting of the absorbance spectra can be seen in Figure 4.4.

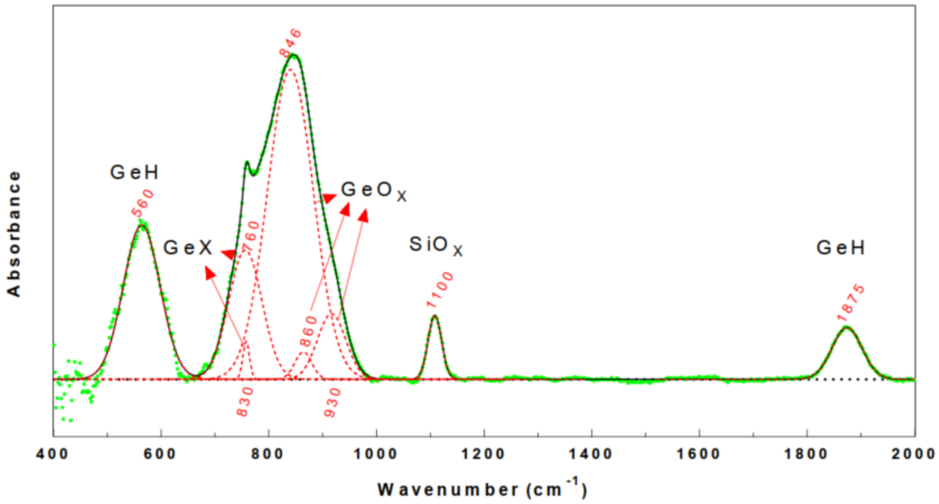

Figure 4.4: Example of the fitted FTIR absorbance spectrum of a typical oxidated Ge:H film.

The bonds in the low-wavenumber range (400-2000 cm^{-1}) were of particular interest in quantifying both the hydrogen concentration in the bulk of the films as well as the comparative level of contamination in the samples, the main parameters extracted from the FTIR study. As mentioned before, hydrogen inclusion in the film plays an important role in both passivating the Ge- dangling bonds and restructuring the large voids in the bulk to lower the defect density of the Ge:H films. The wagging vibration mode of GeH at $\omega \approx 560$ cm^{-1} is used to study the level of hydrogen concentration in the bulk (C_H). The bonds in the range of 800-1050 cm^{-1}, attributed to different Ge-O bonding configuration have been studied to uncover the oxidation level (α_{GeOx}), origin and impact on the electric properties of the films. A complete recapitulation of the atomic bonds in the processed Ge:H films along with their respective sources and vibrational modes can be found in Table 4.1

Table 4.1: FTIR active bonds in Ge:H and their corresponding center frequencies.

Center Frequency (cm^{-1})	**Bond**	**Mode**	**Source**
400	GeH_2	rocking B1	[49] [50]
512	$Ge-O-Ge$	bending, O_2 during deposition	[51]
565	$Ge-H$	wagging	[52]
610	$Ge-C$		[53]
660	Ge_2O_2	surface oxidation of Ge	[49] [50]
670	$Ge-O-Ge-H$	only for samples with O_2 source	[49] [50]
760-765	$GeOx$	oxidation on nc-Ge surface	[53]
820	$Ge-CH_3$	rocking	[54]
820-830	$GeOx$	bending, unstable material	[55]
1100	$Si-O-Si$	stretching	[53] [56]
1640	H_2O	bending	[55]
1870-1875	$Ge-H$	stretching	[49] [50]
1975	$Ge-H_2$	stretching, associated with voids	[49] [50]
2025/2055	O_2GeH	stretching	[55]
2800-3000	$C-H_x$	associated with unstable material	[54]

Hydrogen Concentration and Oxygen Contamination

As mentioned earlier, the area of the absorption peak at $\omega \approx 560\ cm^{-1}$ is used to calculate the hydrogen concentration C_H in the film. The density of the chemical bonds in N_x, is calculated through a constant A_x. A_x is a proportionality constant empirically extracted in other studies. For the purpose of calculating the C_H, a value of $1.3 \cdot 10^{19} cm^{-2}$ is used for A_{560} as determined by [57].

$$N_x = A_x I_x = A_x \int \frac{\alpha(\omega)}{\omega} d\omega \tag{4.4}$$

In Equation 4.4, $\alpha(\omega)$ is the absorption coefficient calculated through the absorbance $A(\omega)$ by:

$$\alpha(\omega) = ln(10)\frac{A(\omega)}{d} \tag{4.5}$$

With d the film thickness. Lastly, by assuming all of the hydrogen is single-bonded in Ge-H wagging bonds, the hydrogen concentration is calculated as:

$$C_H = \frac{N_{560}}{N_{Ge}} \tag{4.6}$$

With N_{Ge} being the atomic density of pure germanium, assumed to be around $4.22 \cdot 10^{22}$ [57].

For lack of an A_{GeOx} proportionality constant value, a new parameter $\alpha_{GeOx})$ has been introduced to quantitatively analyse the amount of oxidation in the proccesed films. Because the the bond between germanium and oxygen is identified to have multiple different configurations at roughly $\omega_n = 846\ cm^{-1}$, $860\ cm^{-1}$, $930\ cm^{-1}$ and $1000\ cm^{-1}$, their summed absorption peak areas α_{GeOx} are used as a thickness independent metric:

$$\alpha_{GeOx} = (\sum(A_{GeOx,n}(\omega) \cdot ln(10) \cdot \omega_n^{-1})) \tag{4.7}$$

Note that in Equation 4.7 $A_{GeOx,n}$ denotes the integrated gaussian absorbance area and not the proportionality constant for Ge-Ox chemical bonds in Ge:H films.

4.1.4. Raman Spectroscopy

Raman spectroscopy (RS) measures a shift in the wavelength (Raman Shift) of light occuring when the light interacts with the molecules inside of a material. This is called the Raman effect [58]. The raman shift $\Delta\tilde{\nu}$ (cm^{-1}) is actually equal to the difference in vibrational/rotational energy levels and the virtual energy states in crystals [59] and is calculated as:

$$\Delta\tilde{\nu} = (\frac{1}{\lambda_0} - \frac{1}{\lambda_1}) \tag{4.8}$$

With λ_0 the excitation wavelength and λ_1 the raman spectrum wavelength. The shift in wavelength can be classified into two categories: Stokes and Anti-Stokes based on whether shift in wavelength is up or down.

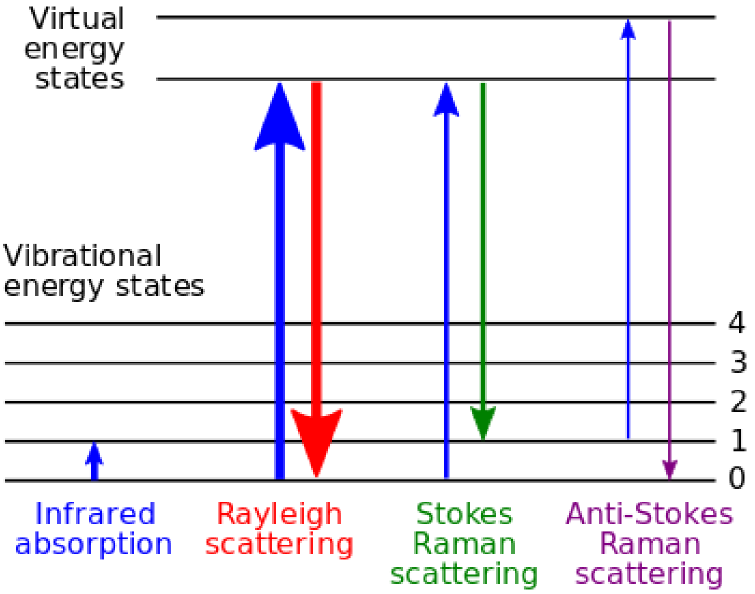

Figure 4.5: Possible inelastic light interactions with a crystal [60].

For this thesis, all RS measurements were done with a Renishaw inVia Raman Microscope, using an Argon laser with an operation wavelength of 514.5 nm. In Ge:H films, RS is able to detect the different Ge-Ge bonds (phonons) and through their respective ratios the crystallinity of the film can be calculated. The RS spectra were normalized to account for variations in laser intensity and then fitted with a constant baseline and 8 different gaussians related to the phonon modes in Table 4.2.

The phonon modes transverse/longitudinal acoustic/optical refer to the movement of the phonon in the lattice. Two optically moving atoms will move in opposite directions (atom 1 moves left, atom 2 moves right and vice versa) while acoustic movement is characterized by the atoms moving in the same direction. Transverse and and longitudinal denote how the phonon moves as a wave through the lattice.

Table 4.2: Raman active phonons in Ge:H and their corresponding center frequencies.

Center Frequency (cm^{-1})	**Bond**	**Phonon Mode**	**Source**
80	a-Ge	TA [transverse acoustic]	[61]
177	a-Ge	LA [logitudinal acoustic]	[61]
230	a-Ge	LO [transverse optic]	[61]
278	a-Ge	TO [transverse optic]	[62] [63]
297-300	nc-Ge	localized optical phonons in Ge nanocrystals	[64] [65]
295	c-Ge	single crytal Ge, non-symmetric	[66]
300.7	c-Ge	single crystal Ge	[67] [62]

Raman Crystallinity

As briefly mentioned, the most important parameter extracted from RS is the Specific Raman Crystallinity X_c. X_c is calculated as:

$$X_c = \frac{I_{300} + I_{295}}{I_{300} + I_{295} + \gamma I_{278}} \tag{4.9}$$

With I_x the area of the gaussian fit at center frequency x. It should be noted that in specifying X_c, the TO phonon is assumed to characterize all amorphous phonon vibrations in the lattice [68]. Analogous to how only the Ge-H wagging bonds were used to specify hydrogen concentration in Section 4.1.3 The correction factor γ is chosen to be equal to 0.85. A value in between $\gamma = 0.8$ commonly used for a-Si:H films and $\gamma = 1$ used for a-Ge:H films in [69].

4.2. Electrical Characterization

4.2.1. Conductivity

The conductivity of a semiconductor is characterized by the concentration, mobility and type of free charge carriers given by:

$$\sigma = e(\mu_e n + \mu_h p) \tag{4.10}$$

With μ_e/μ_h the electron/hole mobilities and n/p the electron/hole concentrations respectively. When no external energy is provided to the semiconductor, the charge carrier densities at thermal equilibrium n_0 and p_0 are given by:

$$n_0 = N_c exp(E_F - E_C)/kT \tag{4.11}$$

$$p_0 = N_v exp(E_V - E_F)/kT \tag{4.12}$$

Where T is absolute temperature and k is the Boltzmann constant. N_c and N_v denote the effective DOS in the CB and VB respectively. On their own, N_c and N_v again are dependent on the temperature through:

$$N \propto T^{3/2} \tag{4.13}$$

Considering an n-type material with $n \gg p$, Equation 4.10 can be simplified to :

$$\sigma = e\mu_e n \tag{4.14}$$

When the temperature is increased, the exponential part of Equation 4.10 is reduced while the DOS near the band edges increases and the conductivity is increased. Using Equations 4.11 and 4.14 the relation between the activation energy $E_a = (E_C - E_F)$ and dark conductivity can be expressed as:

$$\sigma_d(T) = \sigma_0 exp(\frac{-E_A}{kT}) \tag{4.15}$$

Commonly known as the Arrhenius equation [70]. The dark conductivity at room temperature (σ_d) was determined using a Keithley 617 electrometer and measuring the current at a fixed bias voltage of 10 V in a temperature range of $130°C$ to $60°C$ in decrements of $5°C$. σ_d is then calculated as:

$$\sigma_d = \frac{I}{V} \cdot \frac{1}{bd} \tag{4.16}$$

Where b is a parameter specifying the ratio of the contact length and the gap between the contacts. For this thesis, contact masks with a b value of 40 were used. E_A is found as the slope of $ln(\sigma_d(T))$ in Equation 4.15. The photo conductivity (σ_{ph}) of the samples was calculated by measuring the current at a fixed voltage of 10V, using an AM1.5 solar simulator at an illumination of 100mW $\cdot\, cm^{-2}$ under a controlled temperature of 25 $\circ$ C, again using Equation 4.16.

The dark conductivity can be used in conjunction with previously mentioned methods to compare the defect density in the samples that have been deposited [71]. With a higher dark conductivity generally implying a higher density of defects within the film. The photo-over-dark conductivity σ_{ph}/σ_d specifies the photo-response of the films and gives an invaluable insight into how the films will compare when used as an absorber in devices. The last figure of merit derived from the conductivity measurements, E_{act}, shows where the Fermi level is positioned in the bandgap relative to either the CB or VB. Ideally the activation energy equals half the width of the bandgap such that the semiconductor is intrinsic for integration in PIN solar cells.

4.2.2. Hall Effect

The Hall effect occurs when a semiconductor is placed in a magnetic field (B) and a current (I) is flowing through the material, thereby creating a Lorentz force F_L on the charge carriers in the semiconductor:

$$F_L = qvB \tag{4.17}$$

Where q is the electric charge of the particle and v its velocity. In the semiconductor, the velocity of the charge carriers can be further specified as:

$$v = \frac{I}{nAq} \tag{4.18}$$

With n the charge carrier density and A the cross-section of the film. When the magnetic field B is positioned perpendicular to the current flow in the semiconductor, the Lorentz force on charge carriers is:

$$F_L = \frac{IB}{nA} \tag{4.19}$$

Leading to positive and negative charge carriers being separated from each other, inducing an electric field that is positioned perpendicular to the flow of the current. This electric field and the resulting potential difference over the film make it possible to identify the type and concentration of the majority charge carriers in the film. For this thesis, Hall effect measurements have been done to identify the type of the majority charge carriers in the film to deduce if the Fermi level is CB or VB sided.

5

Deposition Window

In this chapter, the deposition window for Ge:H films will be characterized. This process is necessary prior to the deposition and optimization of Ge:H in order to properly understand the boundaries between which Ge:H processing is both feasible and reproducible in the CASCADE reactor.

5.1. Deposition Parameters

In Section 3.3, the PECVD process and different deposition parameters have been laid out. Those same parameters are used throughout this chapter to identify a desirable processing window for Ge:H films. The work done in [72] has provided a point around which to vary the deposition parameters. The full range for which the deposition window of Ge:H in CASCADE has been assessed can be found in Table 5.1.

Table 5.1: Deposition parameters for obtaining a Ge:H processing window.

Deposition Parameter	**Range**	**Unit**
Hydrogen Dilution Ratio	50-400	-
Deposition Pressure	0.3-7	mbar
Deposition Temperature	200	°C
RF-Power	5-50	W
Electrode distance	20	mm

5.2. Deposition Window Characterization

As mentioned earlier in Section 3.3, the combination of pressure and power could have a big impact on the unformity and formation of the plasma in the reactor and possible polymer formation of the dissociated germane molecules [52]. As such, prior to any film characterization, the plasma during deposition is categorized as follows:

- **No Plasma**: The plasma failed to ignite. Most commonly occurring because the power density between the electrodes is too low. No growth is possible in a plasma-less environment,
- **Stable Plasma**: The plasma during deposition is stable meaning that the reproducibility of the films in this regime is greatly increased
- **Unstable Plasma**: The plasma is flickering during the deposition. The reproducibility of the samples is lowered and confident depositions cannot be done in this regime.

After deposition and before characterization, the samples can be further categorized through a visual inspection of the films as:

- **No Deposition**: No growth is visible on the substrates at this regime. Possibly due to a number of reasons. (Dirty substrates, structure of the substrates, unfavorable deposition conditions, no plasma etc.)
- **Clear Deposition**: A clear deposition is visible on the substrates, either uniform or non-uniform. Deposition of both clear and uniform samples is preferred as the reproducibility in this regime is highest and thus proves best for future integration in devices or further studies.
- **Dusty Deposition:** As explained before, a deposition regime with a very high RF-power and pressure is susceptible to producing films where the radicals in the plasma do not develop on the substrates but rather form polymers/dust particles that settle on the substrates. The sample can be visualized as dusty/cloudy with a non-uniform peelable film. With no confidence in the reproducibility of these depositions, they are not studied in this thesis.

An overview of the explored deposition window as specified can be seen in Figure 5.1. For the purpose of studying the growth and properties of Ge:H films, only clear depositions under a stable plasma have been studied (white area). This area encompasses most depositions done between 5-30 W and 0.5-5 mbar. The shaded area denotes a dust forming regime within CASCADE and specifies the boundaries of the deposition window. It should be noted that for depositions with an RF-power below 5W and a pressure below 0.5 mbar no plasma could be ignited, indicating the lower bounds of the deposition under the conditions in Table 5.1. The crystallinity of the processed films is indicated the size and color of the markers. A crystalline phase in the samples was mostly observed at a high hydrogen dilution ratio D = 400, as was expected. A transition from a-Ge:H and nc-Ge:H with a high crystallinity can be seen in the window ranging from 20-25 W and 3-4 mbar.

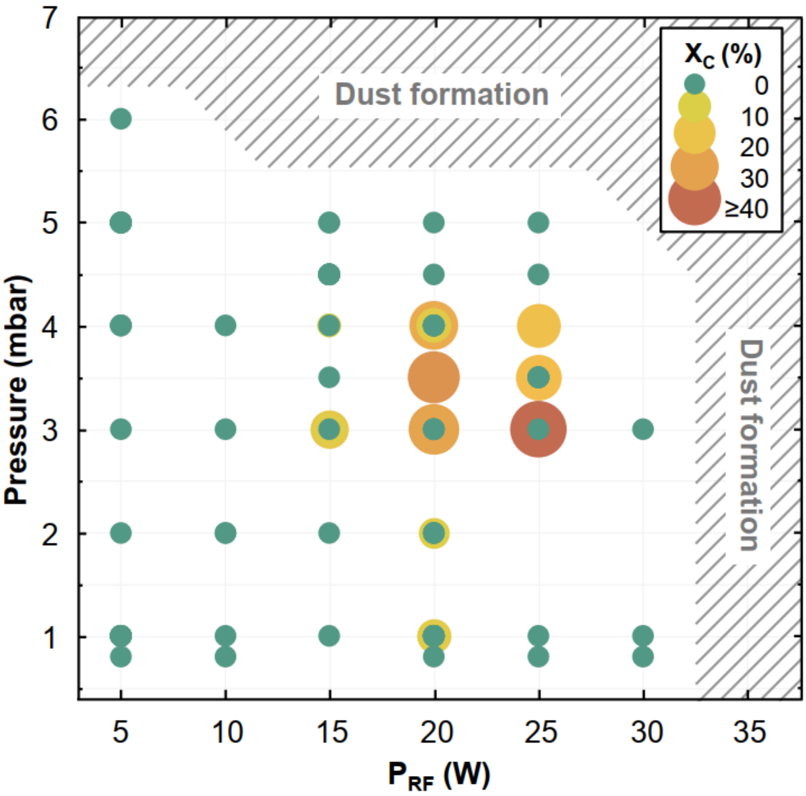

Figure 5.1: Pressure-Power plot for all Ge:H films. The white area denotes a window where clear depositions were made with a stable plasma. The crystallinity of the films is depicted by the size and color of the markers. The shaded area indicates the boundary of the processing window (dusty deposition).

Concluding, a deposition window for clear, stable-plasma depositions has been charted. In addition to that a smaller window for the optimization of nc-Ge:H films has been identified. It has been widely accepted that the material made at the amorphous-to-nc-Si transition yields the best performance in Si solar cells [73] [74]. If the same logic is found to be applicable in germanium processing, the nc-Ge:H processing window should give good insights into the required deposition parameters.

6

Characterization of a-/nc-Ge:H Films

In the previous chapter a deposition window for Ge:H films has been identified over a large range in the deposition parameters. As a result, a good understanding has been developed of the boundaries in Ge:H processing. This chapter splits up the interaction between the different deposition parameters in the hopes of understanding their individual influence on the growth and properties of the films. In Section 6.1 the effect of a varying deposition temperature will be studied. In Section 6.2 the effect of the hydrogen dilution on both the structure of the films and the electrical properties will be discussed. Due to the intricate relation between the pressure and RF power in the formation of the plasma, these two parameters will be studied together in Section 6.3. Lastly, an effort is made in Section 6.4 to understand the extent in which the oxidation of the films affects their opto-electrical properties.

6.1. Effect of Varying Deposition Temperature

The deposition window of Ge:H films has initially been characterized around 200 $°C$, a temperature at which doped silicon layers are processed. The deposition temperature's further effect on film properties should however be studied for germanium films specifically. With germanium having a higher inherent defect density compared to silicon, giving the PECVD process more degrees of freedom when it comes to deposition tunability can potentially result in a much better and complete understanding of the Ge:H films.

To that end, one nc-Ge:H film (3.5mbar 25W) and one a-Ge:H film (4.5mbar 15W) have been processed under varying temperature settings in CASCADE. Both pressure-power combinations are situated in the amorphous-to-crystalline transition regime. Their high σ_{ph}/σ_d ratio's relative to other Ge:H samples make them the better candidates for integration in devices. A complete list of the deposition conditions of the two samples can be found in Table 6.1

Table 6.1: Deposition parameters for one nc-Ge:H and one a-Ge:H film for studying the effect of a varying deposition temperature.

Parameter	**Value/Range**	**Unit**
Pressure-power	3.5-25, 4.5-15	mbar-W
Deposition Temperature	150-200-250-300-350	°C
Electrode Distance	20	mm
Thickness	100	nm
F(H_2)/F(GeH_4)	400,350	-

The variation of different film properties with the deposition temperature is visualised in Figure 6.1. The first point of note is the high deposition rate regardless of deposition temperature T_S. The deposition rate has a lower bound of 6 nm/s and reaches a maximum value of 11 nm/s for the nc-Ge:H sample (blue circle). In earlier chapters, it has already been discussed how the dissociation rate of germane molecules is higher than that of silane, with a higher flux of radicals that are incident on the substrate surface as a result. When compared to a-Si:H growth experiments done within the TU Delft PVMD group, the Ge:H samples show a growth rate that is 1-2 orders of magnitude greater. A higher growth rate may be the cause of large voids in the film. With regards to the temperature, it could be theorised how an elevated substrate temperature may facilitate both dissociation of the germane molecules and surface reactivity of the created radicals[75]. Much like is necessary in thermal CVD processes. While the deposition rate does show a slight increase with increase in temperature for the a-Ge:H samples (black), no clear correlation can be seen for the nc-Ge:H samples (blue). An earlier study on the growth of amorphous germanium has however shown a more conclusive increasing relation between the growth rate and deposition temperature T_S [55]. A further comparison between the growth rate and the refractive index ($n_{@600nm}$) can be drawn to figure out the influence of a very high growth rate of the films. The refractive index can be used a reliable metric in comparing relative porosity of the films. While the nc-Ge:H samples (blue) don't show any intercorrelation with the a-Ge:H samples (black) in deposition rate, both samples show an upwards trend in refractive index with temperature. The a-Ge:H samples show a slightly elevated deposition rate and thus it could be expected that with increasing T_S the films become more porous but the refractive index indicates otherwise. A change in the microstructure of the films through in-situ annealing of the films at higher deposition temperatures could in this case be the process that is counteracting the expected higher porosity of the films at higher deposition temperatures [76]. Weakly bonded hydrogen atoms are defused from the lattice, opening up possibilities for the lattice to restructure.

When looking at the hydrogen concentration C_H as a function of the deposition temperature, a downward trend can be seen for both amorphous and nanocrystalline material. The hydrogen concentration for a-Ge:H has a maximum value of 8% at $T_S = 150\ °C$ and decreases

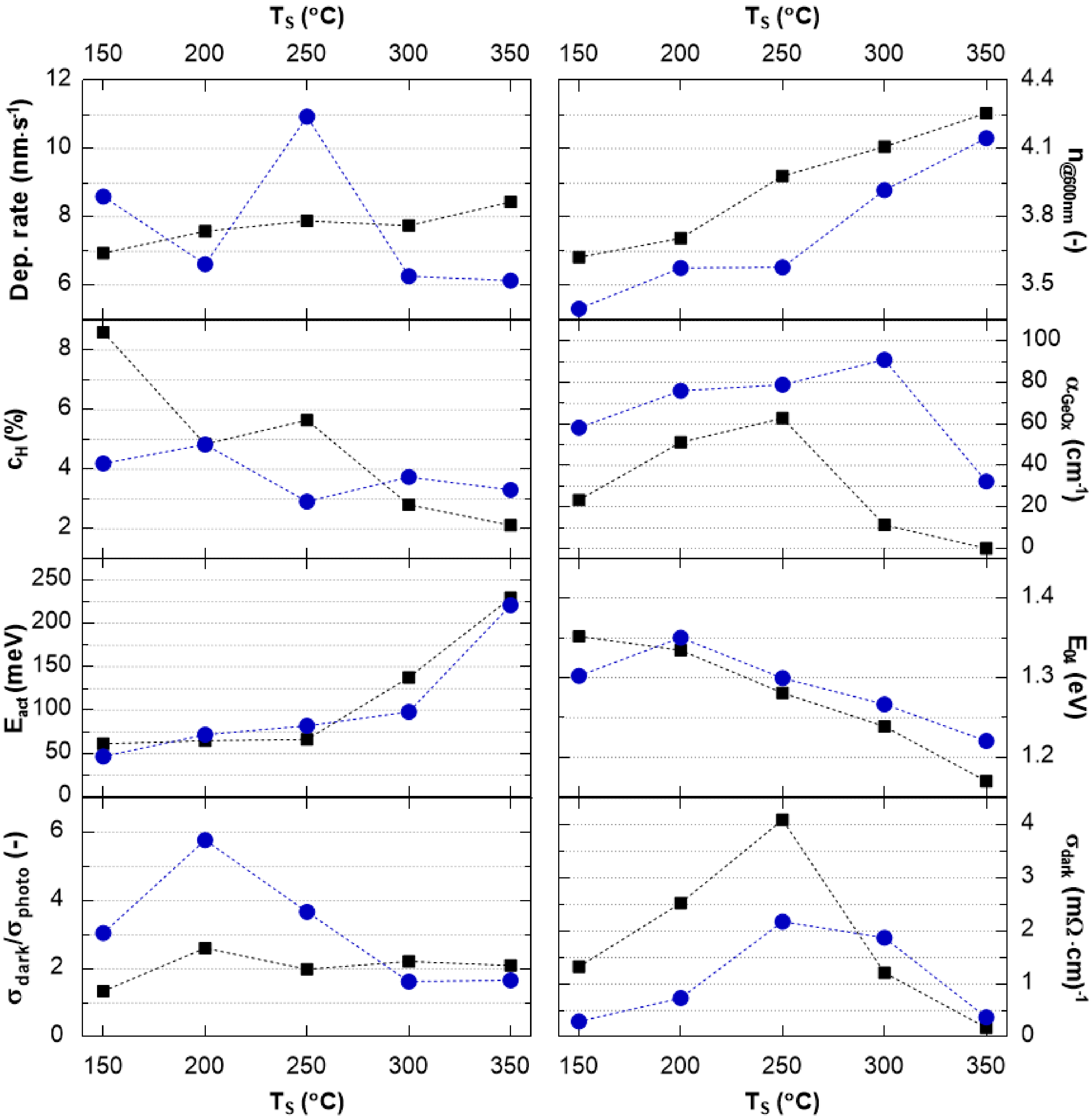

Figure 6.1: Effect of varying substrate temperature on film properties. The blue circles denote the nc-Ge:H films that have been processed at 3.5 mbar, 25 W and a dilution ratio of 400. The black squares denote the a-Ge:H films deposited at 4.5 mbar, 15 W and a dilution ratio of 350.

to 2% at $T_S = 350\ °C$. In addition, the optical bandgap E_{04} of the materials is also decreasing with an increase in the deposition temperature. Ranging from 1.35 eV to 1.15 eV for the amorphous samples. When looking at $n_{@600nm}$, C_H and E_{04} simultaneously, it can be seen how the both the hydrogen concentration and the E_{04} linearly decrease as a function of the refractive index and this is fully in line with the theory laid out in Chapter 2. With a presumed elevated rate at which the weak bulk Ge-H bonds are broken up when the temperature is increased, the lattice can be re-ordened and a denser material ($n_{@600nm}$ is increased) can be grown. As hydrogen has been defused from the bulk of material, the hydrogen concentration is expected to decrease. As a result of both a reduced hydrogen concentration and the restructuring of the lattice, the E_{04} is reduced. However when comparing these results to the crystalline fraction of the films shown in Figure 6.2, there seems to be no clear correlation. While the previous results do suggest that the number of voids per unit volume decrease with an increase in temperature, the trends in the crystalline fractions don't follow.

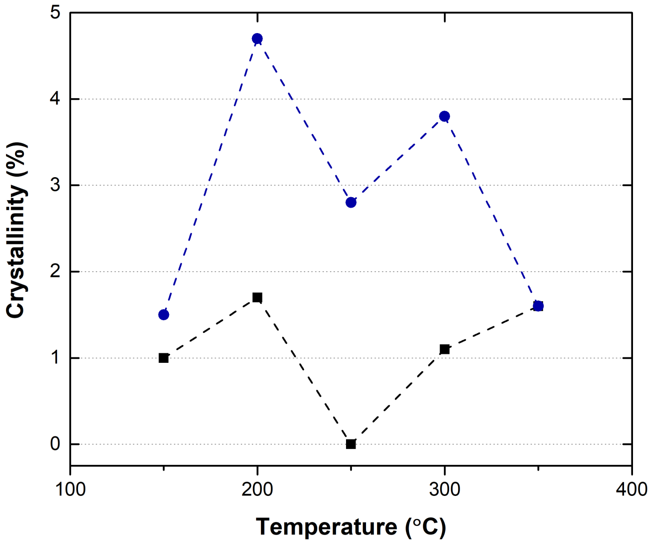

Figure 6.2: Effect of varying substrate temperature on film crystallinity X_C. Blue circles denote nc-Ge:H films at a dilution ratio of 400 and black squares denote a-Ge:H films processed at a dilution ratio of 350.

With less porous films being created at higher temperatures, the expectation is that the films are more resistant to contamination. With less large voids present in the material, the chance in encountering a defect state is assumed to also decrease. It is important to note that the oxidation of films happens post-deposition as opposed to being an in-situ process. This can be backed up by the fact that a large fraction of the Ge:H samples processed did not show any presence of GeOx bonds through infrared measurements right after deposition. Suggesting that oxidation happens in the ambient. To characterize the oxidation of the films as a function of the temperature, Figure 6.1 depicts the summed absorption coefficient of the different GeOx bonds (α_{GeOx}) in the films. α_{GeOx} seems to steadily increase up until it reaches a maximum between a deposition temperature of 250 °C and 300 °C. After which α_{GeOx} rapidly decreases towards a minimum value. When comparing this result to the hydrogen concentration, the initial increase in α_{GeOx} can be correlated with a decreasing C_H. Since hydrogen is effusing from the film, a larger fraction of the Ge dangling bonds is left unpassivated. Open bonds in a-Si:H processing have been shown through FTIR and ESR (electron spin resonance) measurements to be the cause for oxidation of the films when exposed to the ambient [77], and it has been shown that this tendency for oxidation is carried over and amplified for Ge:H processing due to its larger defect density [78]. Past the maximum of α_{GeOx}, its rapid decrease can be correlated with an increase in the material density past a certain threshold value for the oxidation of the films. As is backed up in the previous paragraph through a continuous increase in the refractive index and decrease in the E_{04}. It is believed that the underlying cause of the decrease in the void density is not due to a decrease in the dissociation of larger plasma phase polymers (Ge_2H_6, Ge_3H_8) as is suggested in [52]. But rather due to an increased mobility of the radicals as they diffuse along the substrate surface. It has been stated in Section 3.3.1 how the Ge radicals have a higher reactivity when compared to Si. As such their mobility is reduced when moving along the surface of the sample and they attach to the sample more quickly, leading to a higher void density of the film. With more sites ambient oxygen inclusion as a result. This process is reinforced through a high flux (when compared to silicon processing) of germanium radicals incident on the substrate during the deposition due to the Ge-H bonds dissociating easier than Si-H bonds. An increase in temperature seems to increase the mobility of the Ge-radicals moving along the surface, producing denser films. It is mentioned in [79] how the growth-through-surface-diffusion-model and the incorporation of voids is a function of the growth flux. This readily explains the difference in threshold temperature values for the two different samples as they've been deposited at different pressure-power combinations, influencing the flux of Ge radicals.

When looking at the electrical properties of the Ge:H samples in Figure 6.1, the first point of note is the low activation energy of the samples. E_{act} steadily increases from 50 meV to 100 meV after which it rapidly goes up at a temperature of 250 °C for the amorphous samples and at 300 °C for the nanocrystalline samples. With the E_{04} varying around 1.3 eV, the Fermi level is found to have shifted from the mid gap (0.5-0.7 eV) by a relatively large margin. To first highlight the accuracy of using E_{04} as an approximation to the mobility gap of the samples as opposed to another metric such as E_{TAUC} or E_{03}, Figure 6.3 has been added. It is readily seen how the Tauc gap and the E_{04} optical bandgap share a linear relation, vertically shifted by about 0.2 eV. This makes both metrics good options for approximating and highlighting the trends in the mobility gap of the samples. For this thesis, use of E_{04} has taken preference over the other options.

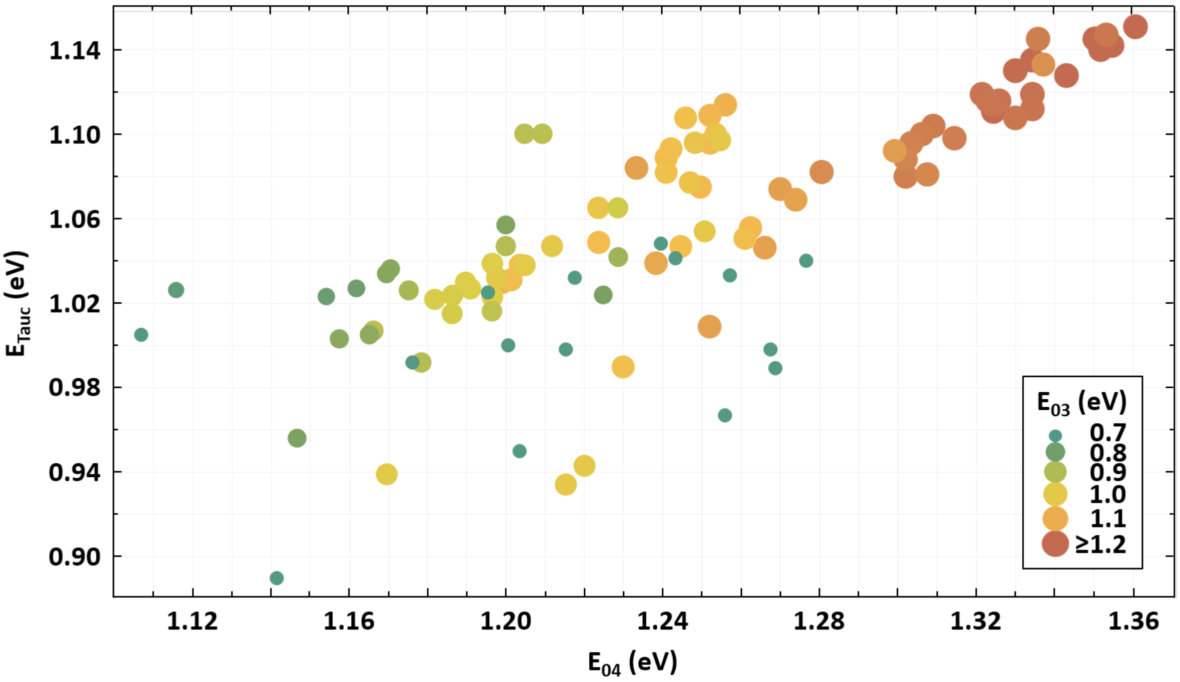

Figure 6.3: Comparison between the relation in E_{04}, E_{TAUC} and E_{03}. E_{03} is denoted by the size and color of the markers.

With such a low activation energy, the germanium samples seem to have a dominant defect type with an energy level close to either the valence or conduction band. There is a strong correlation in the level of oxidation in the films and their corresponding activation energies. The threshold temperatures where E_{act} increases rapidly (250 $°C$ for a-Ge and 300 $°C$ for nc-Ge) match the threshold temperature values for rapid decline in α_{GeOx}. The work done in [80] has suggested that oxidation of a-Ge films introduces defects close to the conduction band. This has been verified with the help of Hall measurements and all of the samples prepared for this thesis have been found to be behaving as n-type. It should be noted however that films with no Ge-O bonds have been measured to have a maximum E_{act} of 260 meV. This is still well below the mid gap, suggesting that the influence of other defect types with energy states below the mid gap play a significant role in reducing the activation energy. Even in the absence of oxygen [81].

The dark conductivity σ_{dark} is shown to increase with an increasing T_S, reaching a maximum between 250 $°C$ and 300 $°C$. As would be expected, the amorphous samples show an overall higher dark conductivity (about factor 2) when compared to the nanocrystalline samples. The random nature of the lattice and subsequent emergence of band tails in the mobility gap make it much more likely for electrons to be randomly excited into the conduction under the absence of sunlight. The average dark conductivity of the samples is orders of magnitude higher when compared to general values for a-Si:H [82] [71]. While this was already expected, it also means that the photo response of Ge:H films in devices will be much lower than Si:H alternatives. Much like it is the case with the activation energy, the dark conductivity seems to be strongly influenced by the films' respective levels of oxidation. σ_{dark} is highest for the samples showing a strong oxidation. Because of the high σ_{dark}, the films show very poor $\sigma_{photo}/\sigma_{dark}$ ratio's, inhibiting their use for device quality purposes.

6.2. Effect of Varying Hydrogen Dilution

From Section 6.1 it has become apparent how the introduced defect states (not necessarily oxygen-induced) are at the forefront of the causes for a low activation energy and deterioration of the films when it comes to their other opto-electrical properties. As we suspect hydrogen may play a leading role in the passivation of any dangling bonds, in this section the influence of hydrogen dilution of the plasma is investigated.

To that end, four samples have been deposited at varying hydrogen dilution ratio's D. Two low pressure samples have been chosen at both a high (20 W) and low (5 W) power to explore a possible regime where the deposition rate can be lowered in order to better control the growth and void inclusion of the films. In addition two high pressure, porous samples have been added close to the a/nc-Ge:H transition regime to explore the effect of hydrogen dilution. A complete list of the deposition parameters can be found in Table 6.2. The variation of the different film properties is visualised in Figure 6.4.

Table 6.2: Deposition parameters for four different Ge:H films for studying the effect of a varying hydrogen dilution ratio's.

Parameter	**Value/Range**	**Unit**
Pressure-Power	1-5, 1-20, 4.5-15, 4-20	mbar-W
Deposition Temperature	200	°C
Electrode Distance	20	mm
Thickness	100	nm
F(H_2)/F(GeH_4)	50-100-150-200-250-300-350-400	-

The deposition rate of the films is still very high. The high pressure films show growth rates ranging from 15 nm/s to 6 nm/s while the low pressure films grow at a reduced rate of about 10 nm/s to 2 nm/s. As a function of the hydrogen dilution, the growth rate is reduced by a factor of 3 over the range. The reduction in growth rate could be a result of the atomic hydrogen etching rate increasing respective to the germanium growth of the film. Alternatively, the growth rate could be simply reduced as a result of there being less germane per unit volume available in the plasma, likely resulting in a lower flux. In the high pressure samples, a slight deviation from the trend is visible around D = 200 and 250. This can be explained through the absolute values of the flow ratio's of the precursors. At D = 200/250, the H_2/GeH_4 flows are changed from 200/1 sccm to 125/0.5 sccm resulting in a sizeable difference in the absolute values of the amount of precursor molecules present in the reactor.

To look at how the structure of the film changes as a function of the hydrogen dilution, Figure 6.5 is added. It is known that the addition of hydrogen to the plasma may help in

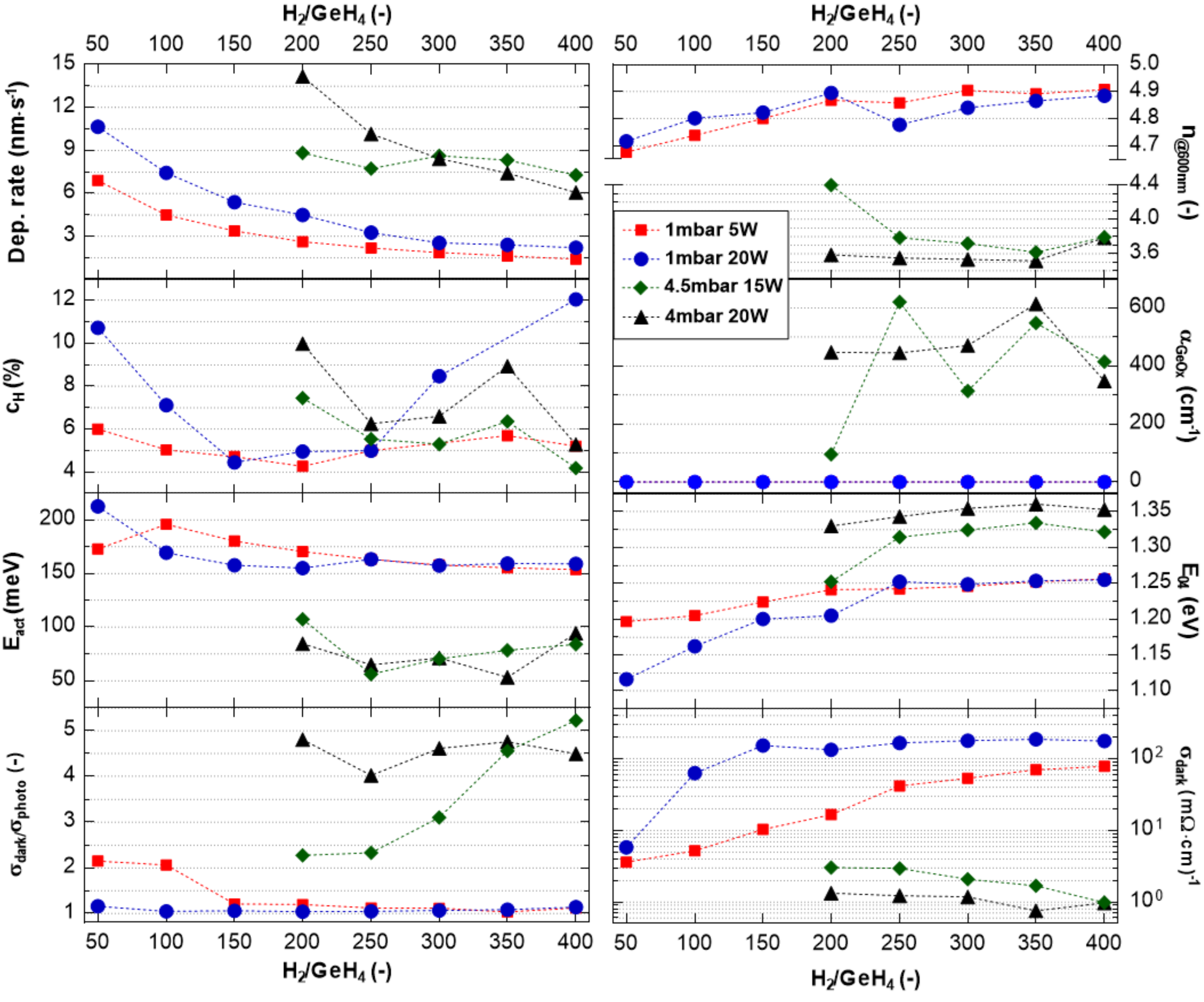

Figure 6.4: Effect of varying hydrogen dilution on film properties. Deposition pressure and power are highlighted in the legend.

restructuring the film to deposit material with a higher crystalline fraction [35]. Looking at the figure, the films are shown to be very amorphous up until the maximum dilution of 400. Especially the 4mbar 20W sample shows a large jump in the crystalline fraction at this point, estimated at around 25%. While it is generally favourable to create material with a higher crystallinity, mainly for the fact that the lattice is more ideal and thus has less voids incorporated into it. This is backed up by the slight increase in the refractive index at the highest dilution ratio. An increased average grain size in the films would normally also point to an improved photo-response of the films [83], though that is not apparent in Figure 6.4. This suggests that there is at least one other growth process influenced by a varying hydrogen dilution that is counteracting the effect a higher crystallinity has on film properties .

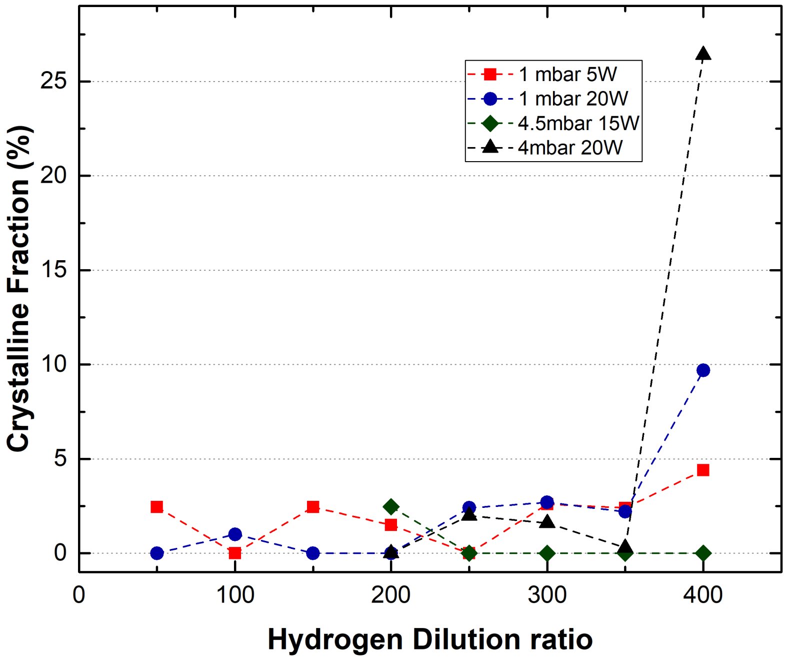

Figure 6.5: Effect of varying hydrogen dilution on crystallinity X_C. Deposition pressure and power are highlighted in the legend.

With a varying dilution of the precursor gasses, the C_H in the films can be expected to change drastically. When looking at Figure 6.4, the hydrogen concentration seems to be decreasing up to a dilution ratio D = 250 for the low pressure samples and D = 300 for the high pressure samples. As such the effect of the dilution ratio can be split up and analysed in two different regimes. A low dilution regime D < 250-300 and a high dilution regime D > 250-300. In the high dilution regime, C_H is increasing drastically for the low pressure-high power sample (blue) while the low pressure-low power sample (red) shows a much more moderate increase in the C_H. This implies that the RF power plays an important role in the incorporation of hydrogen in the films, independent of the hydrogen dilution. The lower power effectively reduces the growth rate which in turn increases the density of the films and thereby reducing the amount of available bonds for hydrogen atoms to latch onto. This conclusion can be further strengthened by looking at the refractive index of the low pressure samples. The low pressure-low power sample (red) shows a lower porosity compared to the low pressure-high power sample (blue), agreeing with he previous statements. The interaction between power and pressure in regards to the film properties is further treated in Section 6.3.

The $n_{@600nm}$ starts to converge to the same value for both blue-red and and black-green sample pairs, where they differ slightly in the lower dilution regime. This suggests that as more and more hydrogen is added to the plasma relative to germane, H atoms in Ge-H bonds in the bulk (only occurring in voids) are extracted and the area around the voids in the lattice can be restructured, resulting in the deposition of denser films. This can also be seen in the E_{act} and E_{04} (both reflective of the defect density in the film) of the samples where they converge to the same value in the high dilution ratio regime. Especially so for the denser films.

The effect of a higher defect density (high porosity, low $n_{@600nm}$) is reflected in the activation energy where the high pressure samples (green and black) show a significantly lower activation energy when compared to the other samples. The difference in activation energies can once again be explained through the oxidation of the films. When looking at α_{GeOX}, the low pressure samples seemingly show no signs of oxygen contamination at any dilution while the high pressure samples show a very large absorption coefficient for IR light in GeOX bonds. As to the underlying reason for the large difference in oxygen contamination of the films, presumably the complex interaction between the increased atomic hydrogen etching, reduced (fractional) availablity of Ge-radicals and less energetic ion bombardement of the film creates favourable growth conditions for growing less porous material, creating fewer sites for the absorption of ambient oxygen into the film. Following that, less oxygen-induced defects with energy levels close to the conduction band are introduced in the mobility gap [68] resulting in a higher activation energy. To further visualize how α_{GeOx} influences the activation energy, note that the 4.5mbar-15W sample at D = 100 shows an α_{GeOx} of 100 cm^{-1} which may seem comparatively low. It is however still a large value in absolute terms as the relation between α_{GeOx} and E_{act} is not necessarily linear. Comparing this data point at D = 200 with the 4mbar-20W sample (black) shows that a difference between $\alpha_{GeOx} = 100\ cm^{-1}$ and $\alpha_{GeOx} = 450\ cm^{-1}$ only increases the activation energy by about 50 meV, which is still nowhere near enough to bring E_{act} to the center of the mobility gap. An further in depth discussion on the relation between the oxidation of the films and other film properties will be presented in Section 6.4.

When looking at the electrical properties of the film, the main point of note is the dark conductivity. σ_{dark} increases slightly with an increase in the hydrogen dilution for the low pressure samples while decreasing for the high pressure samples. Comparing this result to the refractive index, it stands out that the denser films actually exhibit a higher dark conductivity in Figure 6.4. With a lower activation energy, the higher pressure films (black and green) are expected to show a higher dark conductivity but the results contradict these expectations.

Consequently, because of the lowered σ_{dark}, the $\sigma_{photo}/\sigma_{dark}$ ratio is higher for the porous material. It is thought that the oxidation of the films plays a complex role in the electrical behaviour of the films whereby it can both enhance or deteriorate the electrical characteristics of the films.

6.3. Effect of Varying RF Power and Pressure

In the previous section it has been highlighted how a difference in the deposition power and pressure could affect the growth rate substantially and subsequently the void density and tendency to react with the ambient. In order to further characterize how the Ge:H films are deposited under different pressure and power combinations, several samples have been deposited and studied. With an aim of further reducing the rate of growth, and simultaneously optimizing the electrical properties of the films, the films have been processed at a maximum dilution ratio $F(H_2)/F(GeH_4)$ of 400. A complete list of the different deposition parameters of the samples that will be studied in this section can be found in Table 6.3. The properties of the different samples are shown in Figure 6.6

Table 6.3: Deposition parameters for five different Ge:H films in studying the effect of a varying the RF power and pressure.

Parameter	**Value/Range**	**Unit**
RF power	5 - 10 - 15 - 20 - 25	W
Pressure	1 - 2 - 3 - 3.5 - 4 - 4.5	mbar
Deposition Temperature	200	°C
Electrode Distance	20	mm
Thickness	100	nm
F(H_2)/F(GeH_4)	400	-

When looking at Figure 6.6, it becomes apparent that the growth rate increases as a function of the deposition pressure. With a larger flux of Ge radicals at the substrate surface, the films starts growing much faster. Increasing by a factor of four when the pressure is increased to 4.5 mbar from 1 mbar. When looking at the influence of the RF power in the dissociation of the germane molecules, the figure shows that the deposition pressure is leading for the growth rate. This is true up until point where the RF power density in the reactor is no longer large enough to sustain the dissociation of the germane molecules. Especially at a low RF power setting of 5 W, the growth rate starts to taper off and deviate from its linear trend as the extra germane molecules in the reactor are no longer dissociating at a similar rate.

Seeing how the deposition rate increases with an increase in pressure, and taking into account the results from previous sections, a low pressure regime would be beneficial for the purpose of depositing denser films. This assumption seems to be supported by refractive index data. At a low pressure, independent of the RF power, dense films with a refractive index of 4.8 are created. As the pressure is increased, the refractive index and therefore the void density

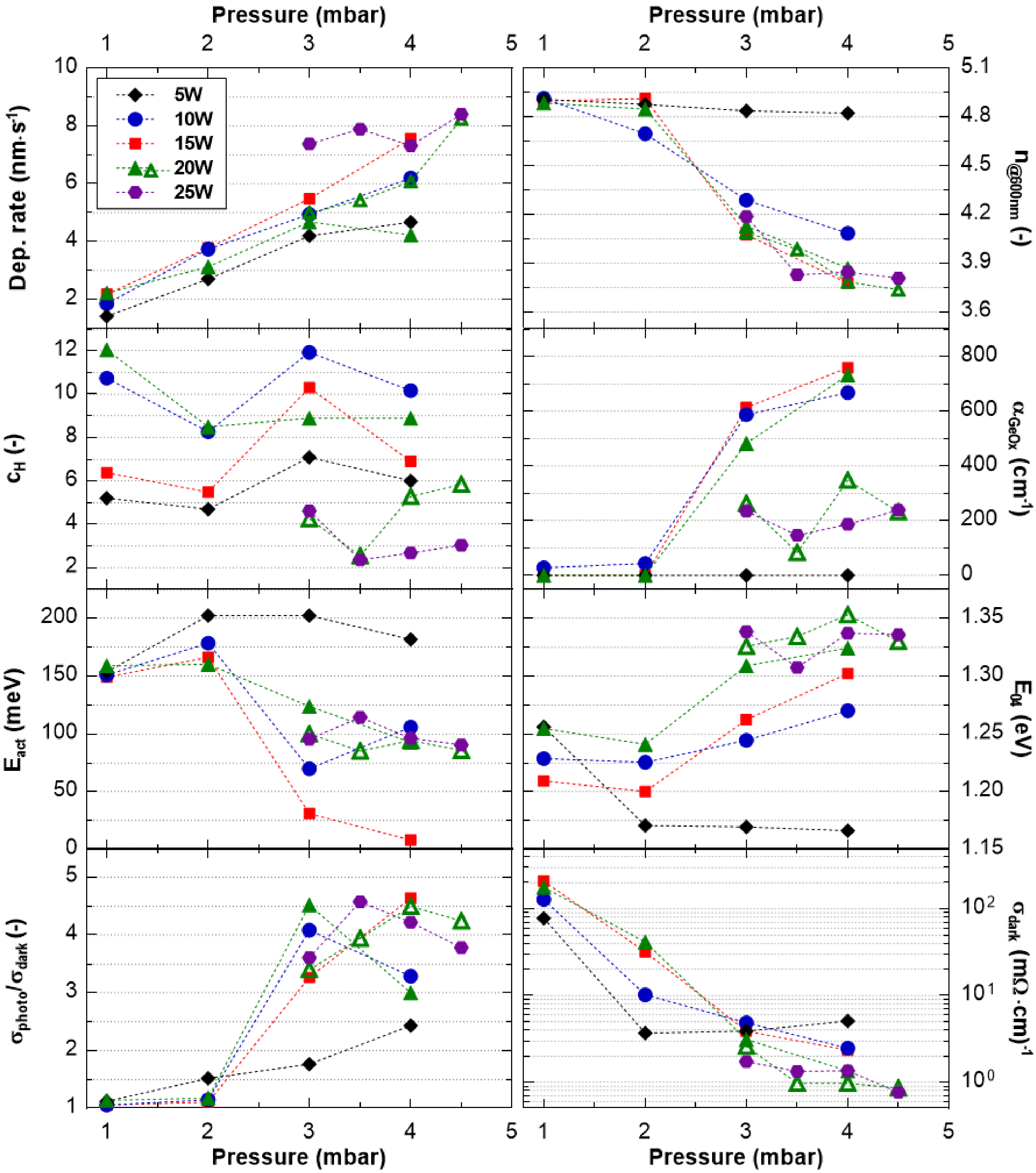

Figure 6.6: Effect of varying the pressure and RF power on film properties.

in the films becomes much more dependent on both RF power and pressure. An increase in the deposition pressure drastically increases the porosity of the films with the slope being determined by the RF power. To further explore the assumptions made, Figure 6.7 is shown. Over a large number of samples, the $n_{@600nm}$ has been depicted as a function of both power and pressure. It is readily seen how a low deposition pressure around 1 mbar produces films with the highest density (dark red). Deposition condition around a pressure of 1 mbar and an RF power of 10 W seem to be optimal for producing films with the highest refractive index. Figure 6.7 seems to corroborate the statement about how a low pressure is typically leading in producing denser films as opposed to to the RF power. Lastly, a combined high pressure and RF power have led to the deposition of the most porous material. It is noteworthy however that from Figure 5.1 it is apparent that this low density regime coincides with the deposition region for nanocrystalline material.

Figure 6.7: Effect of varying the pressure and RF power on the refractive index @ 600 nm over a large sample set. The refractive index is depicted through the size and color of the markers.

With an idea of the influence of the deposition power and pressure on the void density of the films, a correlation can be drawn with the oxidation of the films. α_{GeOx} is shown to be increasing rapidly between a pressure of 2-3 mbar for the samples deposited at an RF power higher than 5 W. This in line with the trends seen in the $n_{@600nm}$ and can thus be contributed to the increased void density of the films at higher pressure-power conditions. What is of particular interest is the tendency of the film deposited at 5 W to stay void of any oxidation for any pressure setting. If the aim of a PECVD process would be to deposit films that are resistant to any oxidation, this would suggest that it is possible to do so even

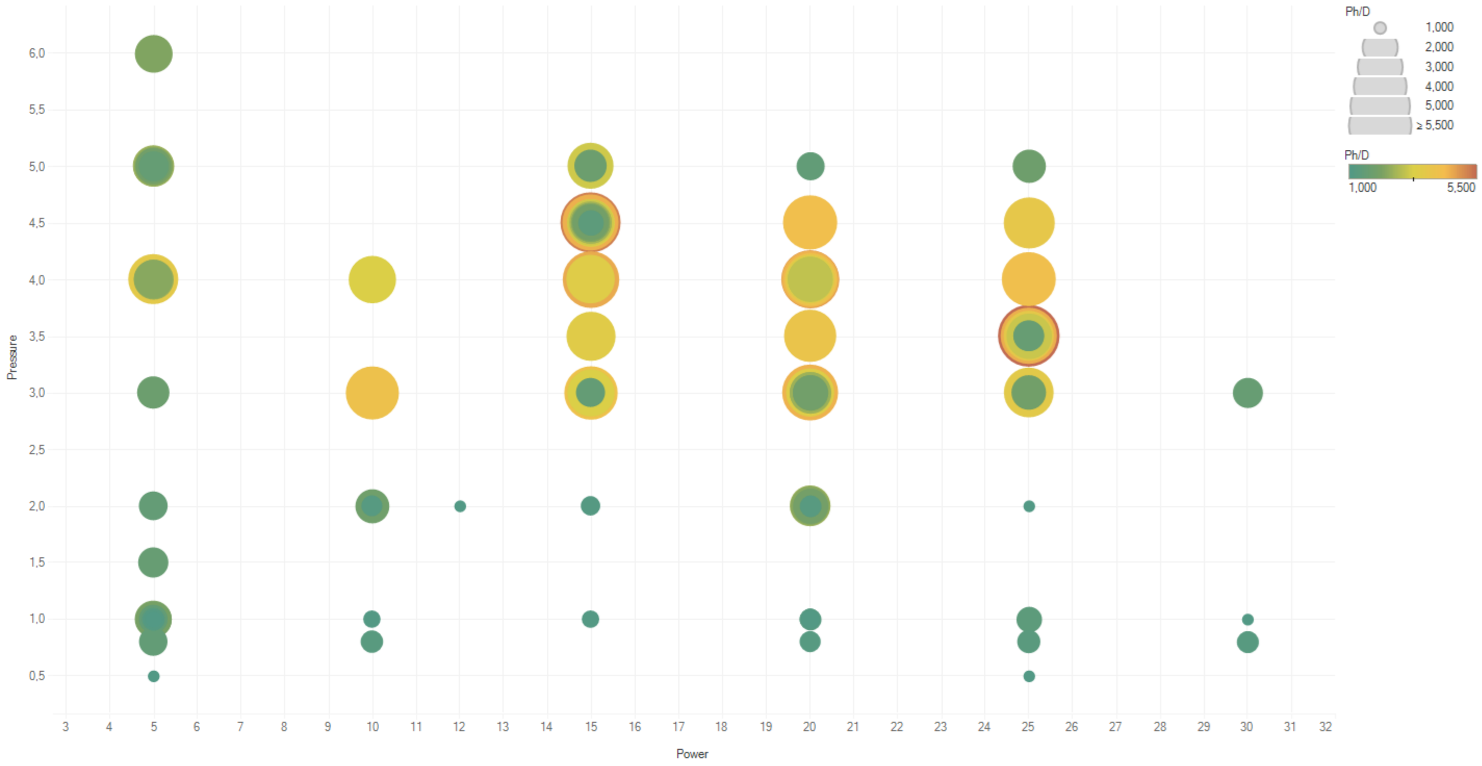

Figure 6.8: Effect of varying the pressure and RF power on the $\sigma_{photo}/\sigma_{dark}$ ratio. $\sigma_{photo}/\sigma_{dark}$ is depicted through the size and color of the markers.

at higher pressures, as long as the RF power is adjusted to a low value. As was observed in Section 6.1, the linear relation between α_{GeOx}, C_H and E_{04} can also be observed in Figure 6.6. As the volume density of GeOx bonds increases in the lattice, so does the volume density of defect states promoting sub bandgap absorption. In turn increasing the E_{04} (more absorption) together with the hydrogen concentration (increase in open bonds for hydrogen to bond with).

When looking at the electrical properties of the films, the E_{act} seems to be once again varying according to the trend in the oxidation of the films. As such as higher seems deposition power and pressure may seem unfavourable in producing intrinsic Ge:H films. When comparing this to the conductivities of the films however, the same points can be raised as in Section 6.2. The films with a higher α_{GeOx}, contrary to the expectations, exhibit an improved photo response over the samples with no oxidation. To confirm this and possibly find more favourable deposition conditions, the $\sigma_{photo}/\sigma_{dark}$ ratio's for a wide range of Ge:H samples have been plotted against the deposition power and pressure. Comparing the results in Figure 6.7 to those in Figure 6.8, it becomes clear that mostly porous films (deposited at a high pressure) show an improved $\sigma_{photo}/\sigma_{dark}$. A deeper discussion into the mechanics of how Ge:H oxidation is affecting the electrical properties of the films is laid out in the next section.

6.4. Post-Deposition Oxidation and Film Properties

From the results in the previous sections, a clear confliction within the growth of Ge:H has surfaced. On the one hand films with a low α_{GeOx} can be produced at lowered growth rates, but the resulting films are show a very low $\sigma_{photo}/\sigma_{dark}$ making them unsuitable for integration in PV devices. On the other hand a higher $\sigma_{photo}/\sigma_{dark}$ is paired with an increase in the oxidation of the samples. An increase photo-response is very appealing but the increased defect density and subsequently the increase in the E_{04} are undesirable when it comes to depositing a low bandgap material. To demonstrate this correlation over a large sample set, Figure 6.9 is shown. As can be seen, no films have been deposited showing both a low α_{GeOx} (green circle) and a high $\sigma_{photo}/\sigma_{dark}$. This would suggest that the opto-electrical of the films (that have been studied until now) is actually dominated through the oxidation as no outliers are present that would indicate a stronger influence of other deposition parameters over the $\sigma_{photo}/\sigma_{dark}$ than the α_{GeOx}.

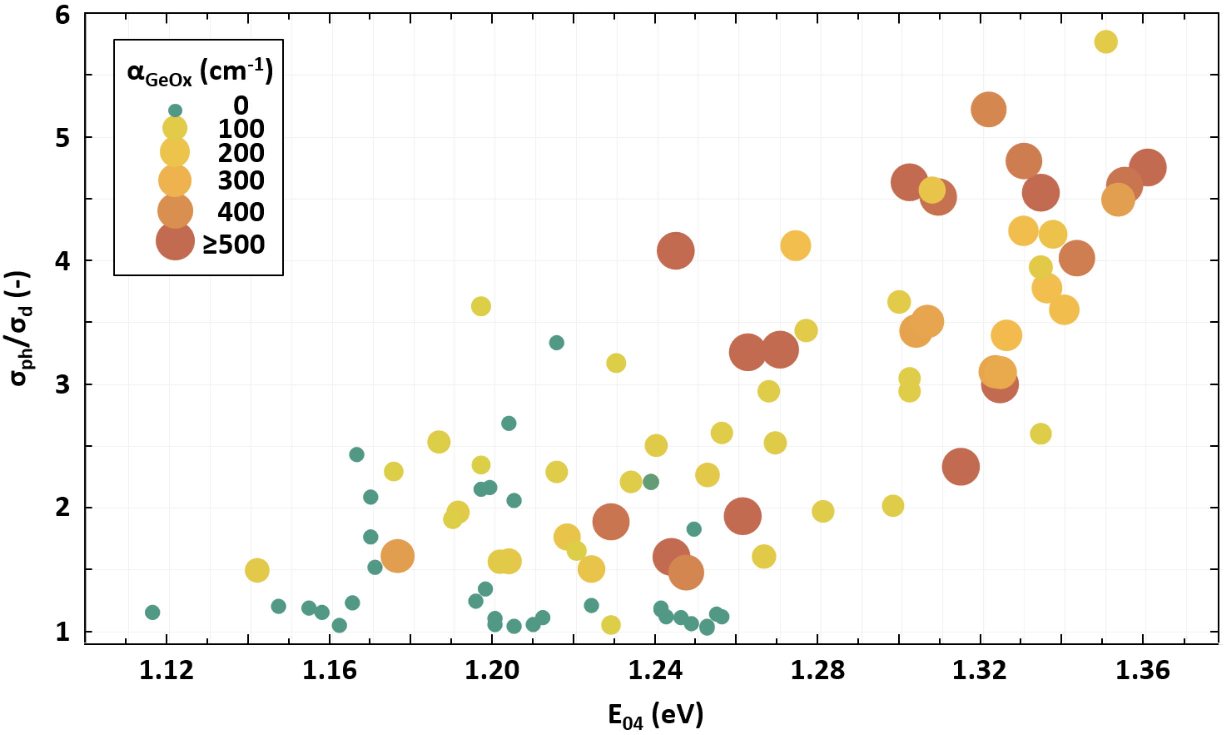

Figure 6.9: Effect of film oxidation on the E_{04} and the $\sigma_{photo}/\sigma_{dark}$ ratio. α_{GeOx} is depicted through the size and color of the markers.

Figure 6.9 also suggests that the E_{04} increases linearly with α_{GeOx}. To further understand how the inclusion of oxygen in the films leads to an increase in the optical bandgap, Figure 6.10 depicts the $\sigma_{photo}/\sigma_{dark}$ and E_{04} as a function of the $n_{@600nm}$. As has been mentioned in previous section, the E_{04} and $n_{@600nm}$ show a strong correlation with the E_{04} increasing when the refractive index is lowered. Comparing this to the oxidation of the films, it seems that only films with a low refractive index are prone to oxidizing. This is possibly due to the decreased material density indicating an increase in the void density. The appearing void defects seem to be close in their energy level to the energy level required for the formation of GeOx bonds. This would insinuate that with an increasing void density (lower $n_{@600nm}$), the oxidation rate should increase along with α_{GeOx} as a result. However, in this case a more continuous increase in the α_{GeOx} would be expected with a decrease in $n_{@600nm}$ compared to the results in Figure 6.10. It is therefore theorized that the agent causing the oxidation in the Ge:H films (presumably H_2O) cannot diffuse into the lattice to react with the available energy sites in the bulk. The diameter of an H_2O molecule is larger than the average lattice constant in denser a-Ge:H films [84] supporting the notion that the water molecules cannot diffuse into high density films to oxidize the bulk. The interplay and causality in the relation between α_{GeOx} and $n_{@600nm}$ are difficult to comment on. A comparison with the Ge:H results to those of an experiment done on the influence of the CO_2 concentration in the precursor gasses for a-SiOx:H (depicted in the inset) is drawn. Here a stronger decrease in the refractive is visible with an increasing CO_2 flow. This difference when compared to the α_{GeOx} results suggest that it might be a combination of a porous Ge:H film inducing the oxidation and simultaneously the oxidation inducing a higher porosity.

In trying to investigate how the photo response of the films is increased through an increase in the α_{GeOx} Figure 6.12 is added. From left to right, the E_{act} (semi-log), σ_0 (log-log), σ_{ph} (log-log) and σ_{ph}/σ_d (semi-log) as a function of the σ_d are plotted. E_{act}, σ_0 and σ_d are related according to Equation 4.15. When looking at the difference between the oxidized (yellow-red markers) and the non-oxidized (green markers) samples in the figure, three big observations can be made: firstly, the σ_{ph}/σ_d increases by a factor 5-6 as the samples oxidize, together with a large decrease in the E_{act} and σ_0. Secondly, the relation of the E_{act} and σ_0 to the σ_d seem to change drastically as the samples move from an non-oxidized to and oxidized regime. Lastly, independent of the α_{GeOx}, the seems to reach maximum value of about 260 meV. A level far below the mid gap energy.

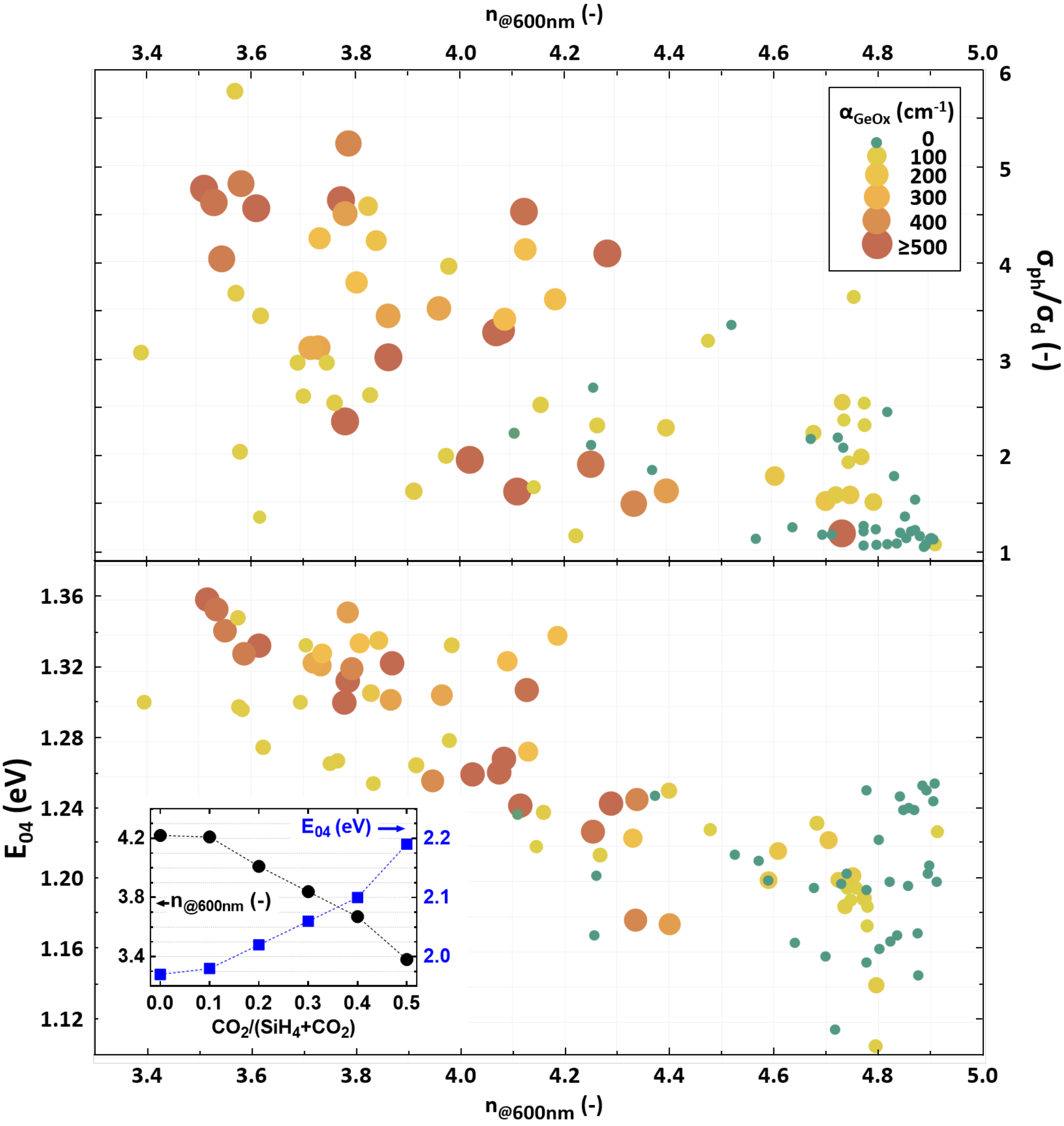

Figure 6.10: $\sigma_{photo}/\sigma_{dark}$ (top) and E_{04} (bottom) plotted as a function of $n_{@600nm}$. α_{GeOx} is denoted by the size and color of the markers. The inset shows $n_{@600nm}$ (black circles) on the left y-axis and E_{04} (blue) on the right y-axis for silicon oxide films as a function of the F(CO_2)/F($SiH_4 + CO_2$) ratio.

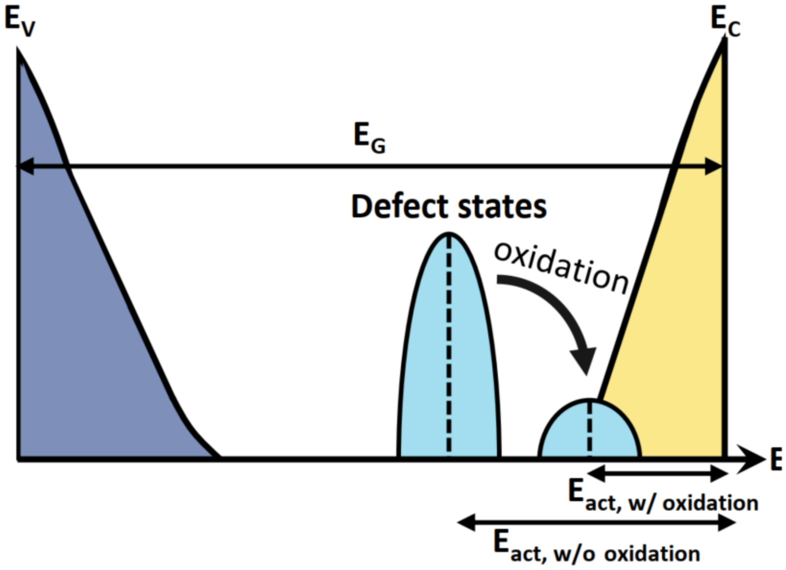

Figure 6.11: Simplified density of states diagram in samples that show both oxidation and no oxidation.

To first explain the increase in the σ_{ph}/σ_d through the decrease in the E_{act} and σ_0, Equation 4.15 is necessary. When looking at Equation 4.15 it can be seen that when the σ_0 remains constant, a slight decrease in the E_{act} should result in an increased σ_d. This happens as a result of electron needing less energy to be promoted to a conductive state. This trend however is only seen in the samples showing no oxidation (green markers) with an E_{act} in the range of 150-250 meV. This increase in the dark conductivity for the non-oxidized samples is however counteracted by an equal increase in the σ_{ph} with a constant value of $\sigma_{photo}/\sigma_{dark} = 1$ as a result. As the α_{GeOx} is further increased, the E_{act} is seen to decrease all the way to 40 meV. The dark conductivity is however not further increased with this decrease in E_{act}. This can be explained by looking at the σ_0. According to Equation 4.15, the influence of σ_0 on the σ_d is much higher than that of the activation energy. As σ_0 actually decreases by about 5 orders of magnitude as α_{GeOx} increases, a significantly reduced dark conductivity is measured despite the decrease in E_{act}. The σ_{ph} is shown to be actually decreasing with an increase in α_{GeOx} and as such the increase large increase in the σ_{ph}/σ_d can be attributed to a very low σ_d rather than a high σ_{ph}. Secondly, the question is raised how the oxidation of the Ge:H films is able to influence both the σ_0 and the E_{act}, with a reduced σ_d as a result. The lowered σ_0 and σ_d suggest that the incorporation of oxygen into the films actually passivate the Ge-dangling bonds within the lattice, decreasing the density of localized defect states. The newly formed GeOx complexes have an energy level much closer to the CB, subsequently shifting the Fermi level closer to the CB as well and decreasing the E_{act}. Figure 6.11 visualizes this phenomenon where a larger defect density is replaced by a smaller defect density positioned closer to the CB. Lastly, a reason for the low E_{act} irrespective of the oxidation in the films is also given. As can be seen in Figure 6.11, without oxidation the DOS diagram is still shown to include a high defect density due to the many unpassivated Ge-dangling bonds, lowering the E_{act} as a result.

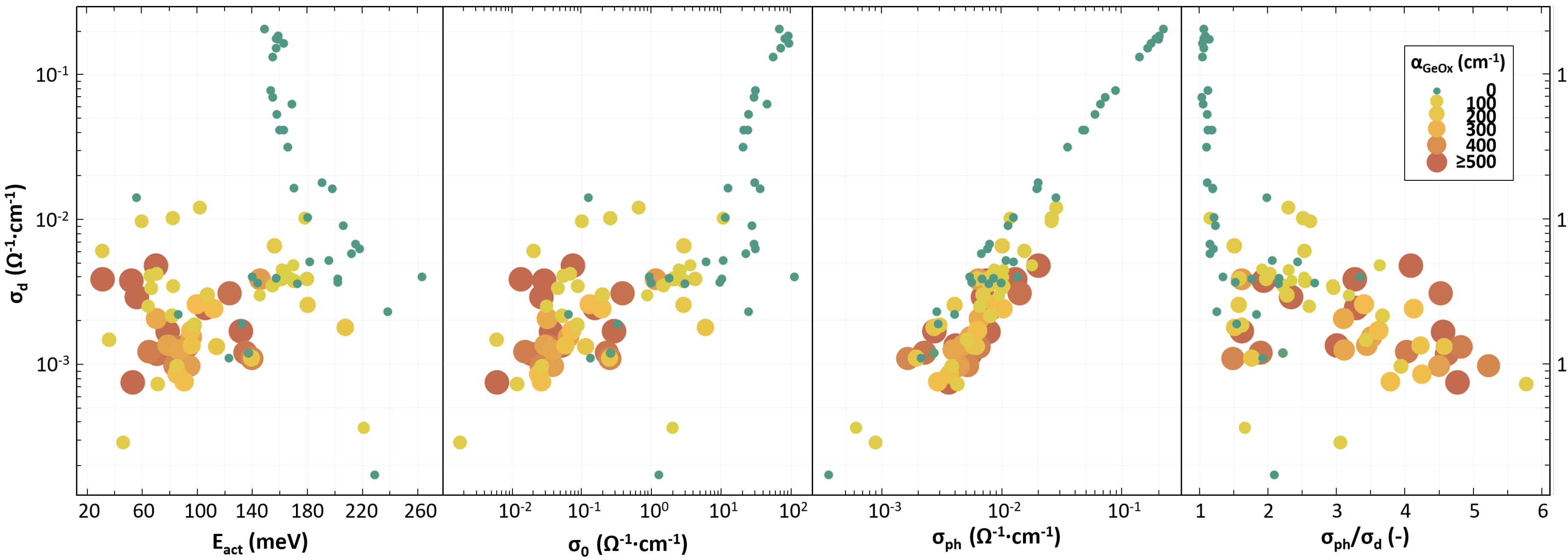

Figure 6.12: E_{act} (left), σ_0 (middle-left), σ_{ph} (middle-right) and the σ_{ph} as a function of the σ_d. The oxidation of the films is depicted through the color and size of the markers.

7

Conclusion and Recommendations

7.1. Conclusion

The goal and aim of this project is to find a deposition regime for Ge:H thin films where device quality films can be deposited. Since no prior data of Ge:H growth within the CASCADE reactor was available, the first research objective within this thesis was to identify a growth window where a stable plasma could be ignited and consequently reproducible Ge:H thin films could be deposited. Secondly, Ge:H films were grown and characterized under a varying temperature, hydrogen dilution and pressure-power setting to investigate their effect on the optical and electrical properties of the films.

A processing window was identified in the range of 1-5 mbar and and 5-30 W RF power at a fixed electrode distance of 20 mm. It was shown that at the boundaries of this processing window the germane precursor starts to polymerize and form larger particles that settle down on the substrate as film rather than breaking up and growing on its surface. The films were found to transition from an amorphous regime to a nanocrystalline regime in the range of 15-25 W at 3-4 mbar, under the highest dilution ratio $F(H_2)/F(GeH_4) = 400$. A crystallinity as high as 54% was reported.

A large fraction of the produced films have shown oxidate post-deposition. The presence and level of oxidation was related back to the refractive index of the films. Low $n_{@600nm}$ indicate porous growth of the Ge:H films. The inclusion and size of voids within the lattice structure of Ge:H make it possible for water within the ambient to diffuse into the material. There the water molecules react with open germanium bonds, increasing the α_{GeOX}. The presence of Ge-O bonds was seen to impact the opto-electrical properties of the films significantly. The E_{04} increases as α_{GeOX} increases, impeding the development of a low bandgap absorber. It was also found that the development of intrinsic Ge:H films is hindered by oxidation of the films. The relation between α_{GeOX} and the activation energy shows that the activation is reduced as more Ge-O bonds are present in the lattice. Films with an activation energy as low as 30 meV have been reported. σ_0 is decreased by 4-5 orders of magnitude. As a result, despite a reduced E_{act}, the dark conductivity is decreased 1-3 orders of magnitude. The underlying mechanism is the increased passivation of Ge-dangling bonds with oxygen atoms. In turn, through a decrease in σ_d rather than an increase in σ_{ph}, the σ_{ph}/σ_d is increased to a maximum of 5-6 for samples with a high α_{GeOX}.

7.2. Recommendations

While this thesis has provided a good first step in explaining the insights and knowledge needed to deposit device quality Ge:H films, a lot of improvements and investigations need to be done before germanium can be properly integrated as a low bandgap absorber.

One of the major points in this thesis has been the deposition of porous films through the easier dissociation of germane when compared to silane. An unstable plasma starts to form in the reactor when the RF power density in the reactor is dropped below a certain threshold. By further decreasing the electrode distance, the power and pressure can be reduced to decrease the growth rate and possibly observe a further increase in the density of the films.

Germanium has traditionally been alloyed with silicon when used as a absorber in solar cells (1.2-1.7 eV). By alloying germanium with tin (0 eV semiconductor) however, the bandgap can be reduced to an energy level below that of c-Ge. The applications and benefits of GeSn alloys have been demonstrated in the field of photodetectors [85] making the material attractive for further exploration in the field of solar cells.

Lastly, the development of single junction cells with a germanium absorber could be interesting. By analysing the performance of germanium in solar cells more insight can be gained into the necessary points of improvement for the material.

Bibliography

[1] I. E. Agency, *World Energy Outlook 2019.* 2019.

[2] M. A. MAHMUD, N. Huda, S. Farjana, and C. Lang, "Environmental impacts of solar-photovoltaic and solar-thermal systems with life-cycle assessment," *Energies*, vol. 11, p. 2346, 09 2018.

[3] E. Roman, R. Alonso, P. Ibanez, S. Elorduizapatarietxe, and D. Goitia, "Intelligent pv module for grid-connected pv systems," *IEEE Transactions on Industrial Electronics*, vol. 53, no. 4, pp. 1066–1073, 2006.

[4] D. Gielen, "Renewable energy technologies: cost analysis series," *Sol Photovolt*, vol. 1, 01 2012.

[5] J. P. Gambino, "Thin silicon wafer processing and strength characterization," in *Proceedings of the 20th IEEE International Symposium on the Physical and Failure Analysis of Integrated Circuits (IPFA)*, pp. 199–207, 2013.

[6] M. Schultz, "Silicon: Semiconductor properties," *Infrared Physics*, vol. 4, no. 2, pp. 93 – 112, 1964.

[7] L. C. Andreani, A. Bozzola, P. Kowalczewski, M. Liscidini, and L. Redorici, "Silicon solar cells: toward the efficiency limits," *Advances in Physics: X*, vol. 4, no. 1, p. 1548305, 2019.

[8] A. ABERLE, "Fabrication and characterisation of crystalline silicon thin-film materials for solar cells," *Thin Solid Films*, vol. 511–512, pp. 26–34, 07 2006.

[9] NREL, "Cadmium telluride solar cells," 2012. `https://www.nrel.gov/pv/cadmium-telluride-solar-cells.html#:~:text=PV%20solar%20cells%20based%20on,thin%2Dfilm%20module%20production%20worldwide.&text=Together%2C%20the%20CdTe%2C%20intermediate%2C,back%20to%20form%20electrical%20contacts.`, Last accessed on 2020-07-05.

[10] M. Zeman, *Advanced Amorphous Silicon Solar Cell Technologies*, ch. 5, pp. 173–236. John Wiley Sons, Ltd, 2006.

[11] NREL, "Copper indium gallium diselenide solar cells," 2012. `https://www.nrel.gov/pv/copper-indium-gallium-diselenide-solar-cells.html`, Last accessed on 2020-07-05.

[12] S. Kim, M.-S. Park, D.-M. Geum, H. Kim, G. Ryu, H. Yang, J. Song, C. Kim, and W. J. Choi, “Fabrication and characterization of single junction gaas solar cell epitaxially grown on si substrate,” *Current Applied Physics*, vol. 15, 04 2015.

[13] R. King, N. Karam, J. Ermer, N. Haddad, P. Colter, T. Isshiki, H. Yoon, H. Cotal, D. Joslin, D. Krut, R. Sudharsanan, K. Edmondson, B. Cavicchi, and D. Lillington, “Next-generation, high-efficiency iii-v multijunction solar cells,” pp. 998 – 1001, 02 2000.

[14] K. Atluri, S. M. Hananya, and B. Navothna, “Performance of rooftop solar pv system with crystalline solar cells,” in *2018 National Power Engineering Conference (NPEC)*, pp. 1–4, 2018.

[15] G. Martino, *Effect of Germanium in Silicon for Solar Application.* PhD thesis, 2016.

[16] M. A. Rind, *Photovoltaic Application of Si and Ge Thin Films DEposited by PECVD.* PhD thesis, 2014.

[17] C. Godet, Y. Bouizem, L. Chahed, I. El Zawawi, M. L. Thèye, M. Meaudre, R. Meaudre, S. Basrour, and J. C. Bruyère, “Band tails and deep-defect density of states in hydrogenated amorphous germanium,” *Phys. Rev. B*, vol. 44, pp. 5506–5509, Sep 1991.

[18] B. Ebersberger, W. Krühler, W. Fuhs, and H. Mell, “Equilibrium defect density in hydrogenated amorphous germanium,” *Applied Physics Letters*, vol. 65, pp. 1683–1685, Sept. 1994.

[19] G. Pennington, N. Goldsman, J. M. McGarrity, and F. Crowne, “A physics-based empirical pseudopotential model for calculating band structures of simple and complex semiconductors,” in *2000 International Conference on Simulation Semiconductor Processes and Devices (Cat. No.00TH8502)*, pp. 229–232, 2000.

[20] L. Lamontagne *Mrl.ucsb.edu*, 2016.

[21] B. S. Alharthi, *Growth and Characterization of SiliconGermanium-Tin Semiconductors for Future Nanophotonics Devices.* PhD thesis, 2018.

[22] W. G. Vandenberghe, B. Sorée, W. Magnus, M. V. Fischetti, A. S. Verhulst, and G. Groeseneken, “Two-dimensional quantum mechanical modeling of band-to-band tunneling in indirect semiconductors,” in *2011 International Electron Devices Meeting*, pp. 5.3.1–5.3.4, 2011.

[23] G. Hodes and P. Kamat, “Understanding the implication of carrier diffusion length in photovoltaic cells,” *The Journal of Physical Chemistry Letters*, vol. 6, pp. 4090–4092, 10 2015.

[24] A. Dey and D. Das, “Optimization of growth of nanocrystalline silicon germanium thin films synthesized by rf-pecvd,” vol. 1942, p. 080069, 04 2018.

[25] E. A. Davis and N. F. Mott, “Conduction in non-crystalline systems v. conductivity, optical absorption and photoconductivity in amorphous semiconductors,” *The Philosophical Magazine: A Journal of Theoretical Experimental and Applied Physics*, vol. 22, no. 179, pp. 0903–0922, 1970.

[26] Y. Liu, *High growth rate deposition of hydrogenated amorphous silicon-germanium films and devices using ECR-PECVD.* PhD thesis, 2002.

[27] T. Shimizu, “Staebler-wronski effect in hydrogenated amorphous silicon and related alloy films,” *Japanese Journal of Applied Physics*, vol. 43, pp. 3257–3268, jun 2004.

[28] M. Stuckelberger, M. Despeisse, G. Bugnon, J.-W. Schüttauf, F.-J. Haug, and C. Ballif, “Comparison of amorphous silicon absorber materials: Light-induced degradation and solar cell efficiency,” *Journal of Applied Physics*, vol. 114, no. 15, p. 154509, 2013.

[29] R. Vanderhaghen, R. Amokrane, D. Han, and M. Silver, “Effect of light-induced degradation on photoconductive gain in a-si:h n-i-p devices,” *Journal of Non-Crystalline Solids*, vol. 164-166, pp. 599 – 602, 1993. Proceedings of the Fifteenth International Conference on Amorphous Semiconductors – Science and Technology.

[30] A. E. Crawford, “A practical introduction to ultrasonic cleaning,” *Ultrasonics*, vol. 1, no. 2, pp. 65 – 69, 1963.

[31] A. F. M. Leenaars, J. A. M. Huethorst, and J. J. Van Oekel, “Marangoni drying: A new extremely clean drying process,” *Langmuir*, vol. 6, no. 11, pp. 1701–1703, 1990.

[32] M. Karaman, M. Gürsoy, T. Uçar, E. Demir, and E. Yenice, “Initiated plasma enhanced chemical vapor deposition (i-pecvd) of poly(alkyl acrylates),” in *2015 IEEE International Conference on Plasma Sciences (ICOPS)*, pp. 1–1, 2015.

[33] J. M. w, *Novel Concepts in the PECVD Deposition of Silicon Thin Films : from Plasma Chemistry to Photovoltaic Device Applications.* PhD thesis, 2018.

[34] R. F. Foster, J. T. Hillman, and R. Arora, “Method and apparatus for low temperature deposition of cvd and pecvd films,” May 13 1997. US Patent 5,628,829.

[35] S.-H. Qiu, C.-Z. Chen, C.-Q. Liu, Y.-D. Wu, P. Li, X.-Y. Lin, C. Huang, and C.-Y. Yu, “Effect of hydrogen dilution on crystalline properties of nano-crystalline silicon thin films in fast growth,” *Wuli Xuebao/Acta Physica Sinica*, vol. 58, pp. 565–569, 01 2009.

[36] J. Van den Heuvel, M. Geerts, and J. Metselaar, “The relation between the optical properties and the hydrogen concentration in a-si: H,” *Solar energy materials*, vol. 22, no. 2-3, pp. 185–194, 1991.

[37] D. Caschera, P. Cossari, F. Federici, S. Kaciulis, A. Mezzi, G. Padeletti, and D. Trucchi, “Influence of pecvd parameters on the properties of diamond-like carbon films,” *Thin*

Solid Films, vol. 519, no. 12, pp. 4087 – 4091, 2011. Carbon- or Nitrogen-Containing Nanostructured Composite Films.

[38] X. Wu, Z. Zhang, Y. Liu, X. Chu, and Y. Li, “Process parameter selection study on sinx:h films by pecvd method for silicon solar cells,” *Solar Energy*, vol. 111, pp. 277 – 287, 2015.

[39] L. Ravangave and S. Jadhav, “Influence of substrate temperature on structure, morphology and optical properties of spray deposited zno thin films,” *JOURNAL OF ADVANCED APPLIED SCIENTIFIC RESEARCH*, vol. 2, no. 3, pp. 1–6, 2020.

[40] S. Prayogi, Ayunis, Kresna, Y. Cahyono, Akidah, and D. Darminto, “Analysis of thin layer optical properties of a-si:h p-type doping ch 4 and p-type without ch 4 is deposited pecvd systems,” *Journal of Physics: Conference Series*, vol. 853, p. 012032, 05 2017.

[41] B. Tillack and J. Murota, “6 - silicon–germanium (sige) crystal growth using chemical vapor deposition,” in *Silicon–Germanium (SiGe) Nanostructures* (Y. Shiraki and N. Usami, eds.), Woodhead Publishing Series in Electronic and Optical Materials, pp. 117 – 146, Woodhead Publishing, 2011.

[42] S. Guha, J. Yang, S. J. Jones, Y. Chen, and D. L. Williamson, “Effect of microvoids on initial and light-degraded efficiencies of hydrogenated amorphous silicon alloy solar cells,” *Applied Physics Letters*, vol. 61, pp. 1444–1446, Sept. 1992.

[43] V. L. Dalal, S. Kaushal, Jun Xu, and K. Han, “A critical review of the growth and properties of a-(si,ge):h,” in *Proceedings of 1994 IEEE 1st World Conference on Photovoltaic Energy Conversion - WCPEC (A Joint Conference of PVSC, PVSEC and PSEC)*, vol. 1, pp. 464–467 vol.1, 1994.

[44] W. Luft, “Characteristics of hydrogenated amorphous silicon-germanium alloys,” in *Conference Record of the Twentieth IEEE Photovoltaic Specialists Conference*, pp. 218–223 vol.1, 1988.

[45] Y. Liu, “High growth rate deposition of hydrogenated amorphous silicon-germanium films and devices using ecr-pecvd,”

[46] “Thermal Evaporation, howpublished = `https://www.sciencedirect.com/topics/agricultural-and-biological-sciences/thermal-evaporation`, note = Accessed: 2020-07-15.”

[47] D. Mergel and M. Jerman, “Density and refractive index of thin evaporated films,” *Chinese Optics Letters*, vol. 8, pp. 67–72, 04 2010.

[48] Z. Remes, R. Vasudevan, K. Jarolimek, A. Smets, and M. Zeman, “The optical spectra of a-si:h and a-sic:h thin films measured by the absolute photothermal deflection spectroscopy (pds,” *Solid State Phenomena*, vol. 213, pp. 19–28, 2014. Harvest Available online 24-3-2014.

[49] T. Matsumoto, Y. Murata, and J. Watanabe, “Study of silicon-hydrogen bonds at an amorphous silicon/silicon nitride interface using infrared attenuated total reflection spectroscopy,” *Applied Physics Letters*, vol. 60, no. 16, pp. 1942–1944, 1992.

[50] M. Cardona, “Vibrational spectra of hydrogen in silicon and germanium,” *physica status solidi (b)*, vol. 118, no. 2, pp. 463–481, 1983.

[51] C. Viana, S. da, N. Morimoto, and O. Bonnaud, “Analysis of sio2 thin films deposited by pecvd using an oxygen-teos-argon mixture,” *Brazilian Journal of Physics*, vol. 31, 06 2001.

[52] G. Lucovsky, S. S. Chao, J. Yang, J. E. Tyler, R. C. Ross, Czubatyj, and W., “Chemical bonding of hydrogen and oxygen in glow-discharge–deposited thin films of a-ge:h and a-ge:(h,o),” *Phys. Rev. B*, vol. 31, pp. 2190–2197, Feb 1985.

[53] W. Paul, “Structural, optical and photoelectronic properties of improved pecvd a-ge:h,” *Journal of Non-Crystalline Solids*, vol. 137-138, pp. 803 – 808, 1991.

[54] C. Hu, L. Qiao, H. Tian, X. Lu, Q. Jiang, and W. Zheng, “Role of carbon in the formation of hard ge1xcx thin films by reactive magnetron sputtering,” *Physica B: Condensed Matter*, vol. 406, no. 13, pp. 2658 – 2662, 2011.

[55] T. Nakashita, A. Inoue, S. Hagiwara, F. Uehara, and K. Kohno, “Dependence of electronic properties of hydrogenated amorphous ge on deposition condition,” *Japanese Journal of Applied Physics*, vol. 31, pp. 1730–1736, jun 1992.

[56] P. Kazimierski and L. Jozwiak, “Transition from amorphous semiconductor to amorphous insulator in hydrogenated carbon–germanium films investigated by ir spectroscopy,” *Journal of Non-crystalline Solids - J NON-CRYST SOLIDS*, vol. 355, pp. 280–286, 02 2009.

[57] M. S. Abo-Ghazala and S. A. Hazrny, “Hydrogen bonding in hydrogenated amorphous germanium,” *Tsinghua Science and Technology*, vol. 9, no. 2, pp. 177–180, 2004.

[58] J. Popp, B. Dietzek, M. Schmitt, P. Rösch, R. Möller, and C. Krafft, “Raman spectroscopy - an essential tool for biophotonics,” in *2011 International Workshop on Biophotonics*, pp. 1–3, 2011.

[59] G. Li, M. Chen, and T. Wei, “Application of raman spectroscopy to detecting organic contaminant in water,” in *2009 IITA International Conference on Control, Automation and Systems Engineering (case 2009)*, pp. 493–495, 2009.

[60] “Raman Spectroscopy, howpublished = `https://en.wikipedia.org/wiki/raman_spectroscopy`, note = Accessed: 2020-06-10.”

[61] D. Bermejo and M. Cardona, “Raman scattering in pure and hydrogenated amorphous germanium and silicon,” *Journal of Non-Crystalline Solids*, vol. 32, no. 1, pp. 405 – 419, 1979. Electronic Properties and Structure of Amorphous Solids.

[62] V. A. Volodin, G. K. Krivyakin, G. D. Ivlev, S. L. Prokopyev, S. V. Gusakova, and A. A. Popov, “Crystallization of Amorphous Germanium Films and Multilayer a-Ge/a-Si Structures upon Exposure to Nanosecond Laser Radiation,” *Semiconductors*, vol. 53, pp. 400–405, Mar. 2019.

[63] Y.-P. Chou and S.-C. Lee, “Structural, optical, and electrical properties of hydrogenated amorphous silicon germanium alloys,” *Journal of Applied Physics*, vol. 83, no. 8, pp. 4111–4123, 1998.

[64] Y. Maeda, “Visible photoluminescence from nanocrystallite ge embedded in a glassy sio_2 matrix: Evidence in support of the quantum-confinement mechanism,” *Phys. Rev. B*, vol. 51, pp. 1658–1670, Jan 1995.

[65] V. Volodin, D. Marin, V. Sachkov, E. Gorokhov, H. Rinnert, and M. Vergnat, “Applying an improved phonon confinement model to the analysis of raman spectra of germanium nanocrystals,” vol. 118, 12 2013.

[66] P. Klement, C. Feser, B. Hanke, K. v. Maydell, and C. Agert, “Correlation between optical emission spectroscopy of hydrogen/germane plasma and the raman crystallinity factor of germanium layers,” *Applied Physics Letters*, vol. 102, no. 15, p. 152109, 2013.

[67] P. Alfaro-Calderon, M. Cruz-Irisson, and C. Wang-Chen, “Theory of raman scattering by phonons in germanium nanostructures,” *Nanoscale Research Letters*, vol. 3, pp. 55–59, 02 2008.

[68] Y. Yamashita, N. Ikeno, N. Aizawa, T. Tachibana, Y. Ohshita, and A. Ogura, “Raman spectroscopy study of crystalline damage induced by pecvd sin,” in *2015 IEEE 42nd Photovoltaic Specialist Conference (PVSC)*, pp. 1–3, 2015.

[69] P. Klement, C. Feser, B. Hanke, K. von Maydell, and C. Agert, “Correlation between optical emission spectroscopy of hydrogen/germane plasma and the raman crystallinity factor of germanium layers,” *Applied Physics Letters*, vol. 102, 04 2013.

[70] arrhenius equation an overview | sciencedirect topics, “Arrhenius equation.”

[71] S. Sato, H. Sai, T. Ohshima, M. Imaizumi, K. Shimazaki, and M. Kondo, “Photo- and dark conductivity variations of solar cell quality a-si:h thin films irradiated with protons,” in *2010 35th IEEE Photovoltaic Specialists Conference*, pp. 002620–002624, 2010.

[72] J. Jiang], K. Chen], D. Feng], and D. Sun], “Structural evolution during the crystallization process of germanium films prepared by plasma enhanced chemical vapour deposition,” *Thin Solid Films*, vol. 230, no. 1, pp. 7 – 9, 1993.

[73] B. Yan, G. Yue, X. Xu, J. Yang, and S. Guha, “High efficiency amorphous and nanocrystalline silicon solar cells,” *physica status solidi (a)*, vol. 207, pp. 671 – 677, 03 2010.

[74] S. Zhang, X. Liao, L. Raniero, E. Fortunato, Y. Xu, G. Kong, H. Águas, I. Ferreira, and R. Martins, "Silicon thin films prepared in the transition region and their use in solar cells," *Solar Energy Materials and Solar Cells*, vol. 90, pp. 3001–3008, 11 2006.

[75] "Deposition temperature, an overview." `https://www.sciencedirect.com/topics/engineering/deposition-temperature`. Accessed: 2020-06-27.

[76] A. Bhaduri, P. Chaudhuri, D. L. Williamson, S. Vignoli, P. P. Ray, and C. Longeaud, "Structural and optoelectronic properties of silicon germanium alloy thin films deposited by pulsed radio frequency plasma enhanced chemical vapor deposition," *Journal of Applied Physics*, vol. 104, no. 6, p. 063709, 2008.

[77] H. Ohsaki, K. Miura, and Y. Tatsumi, "Oxidation mechanism of amorphous silicon in air," *Journal of Non-Crystalline Solids*, vol. 93, no. 2, pp. 395 – 406, 1987.

[78] N. Patel, *Understanding Defects in Germanium and Silicon for Optoelectronic Energy Conversion.* PhD thesis, Georgia Institute of Technology, 2016.

[79] A. H. M. Smets, W. M. M. Kessels, and M. C. M. van de Sanden, "Surface-diffusion-controlled incorporation of nanosized voids during hydrogenated amorphous silicon film growth," *Applied Physics Letters*, vol. 86, no. 4, p. 041909, 2005.

[80] M. Moreno, N. Delgadillo, A. Torres, R. Ambrosio, P. Rosales, A. Kosarev, C. Reyes-Betanzo, J. [de la Hidalga-Wade], C. Zuniga, and W. Calleja, "Boron doping compensation of hydrogenated amorphous and polymorphous germanium thin films for infrared detection applications," *Thin Solid Films*, vol. 548, pp. 533 – 538, 2013.

[81] J.-K. Lee and E. A. Schiff, "Modulated electron-spin-resonance measurements and defect correlation energies in amorphous silicon," *Physical Review Letters*, vol. 68, no. 19, pp. 2972–2975, 1992.

[82] A. Klaver, "Irradiation-induced degradation of amorphous silicon solar cells in space," 07 2020.

[83] M. Moreno, R. Ambrosio, ArturoTorres, A. P. Torres, P. Rosales, A. Itzmoyotl, and M. A. Dominguez, "Amorphous, polymorphous, and microcrystalline silicon thin films deposited by plasma at low temperatures," 2016.

[84] T. A. Abtew and D. A. Drabold, "Ab initio models of amorphous $\mathrm{si}_{1-x}\mathrm{ge}_x : \mathrm{H}$," *Phys. Rev. B*, vol. 75, p. 045201, Jan 2007.

[85] H. Tran, C. G. Littlejohns, D. J. Thomson, T. Pham, A. Ghetmiri, A. Mosleh, J. Margetis, J. Tolle, G. Z. Mashanovich, W. Du, B. Li, M. Mortazavi, and S.-Q. Yu, "Study of gesn mid-infrared photodetectors for high frequency applications," *Frontiers in Materials*, vol. 6, p. 278, 2019.